Vilnius University
Faculty of Physics
Institute of Applied Electrodynamics and Telecommunications

Muhammad Shahzaib Asad

TRIBOELECTRIC PROPERTIES OF PDMS-BASED COMPOSITES FILLED WITH FERROELECTRIC PARTICLES

Master's Final Thesis

Electronics and Telecommunication Technologies Study Programme

Student	Muhammad Shahzaib Asad
Approved	2026-05-22
Academic supervisor	dr. Darya Meisak
Director of the Institute	prof. Robertas Grigalaitis

Vilnius 2026

LIST OF ABBREVIATIONS

$BaTiO_3$	Barium Titanate
CE	Contact Electrification
ESD	Energy Storage Device
IPA	Isopropyl Alcohol
ITO-PET	Indium Tin Oxide Coated Polyethylene Terephthalate
NBT-BT	Sodium Bismuth Titanate-Barium Titanate
PDMS	Polydimethylsiloxane
RMS	Root Mean Square
RPM	Revolutions Per Minute
SEM	Scanning Electron Microscopy
TENG	Triboelectric Nanogenerator

CONTENTS

INTRODUCTION

The use of renewable energy is increasing rapidly because of its simple structure and the low cost of the energy generation systems. Triboelectric nanogenerators (TENGs) are very efficient at converting mechanical energy into electrical energy. [1] The mechanism of triboelectric nanogenerators (TENGs) works based on the principles of contact electrification (CE) and electrostatic induction. When two materials with opposite polarities come into contact, they produce surface charges. The separation of these materials yields a potential difference in the transfer of electrons across an external circuit. [2]

The performance of a triboelectric nanogenerator (TENG) is affected by several factors, such as the properties of the material, structure, and the environment in which the device operates. Polydimethylsiloxane (PDMS) is commonly used in triboelectric nanogenerators (TENGs) due to its outstanding flexibility, transparency, and durability. But pure PDMS does not have high output due to its low electrical performance. Therefore, fillers are incorporated into composite films to increase the output. [3] These fillers make the surface rougher and improve the dielectric properties. Moreover, they enhance charge storage capabilities, which leads to a higher output. [4]

Barium Titanate ($BaTiO_3$) is widely used in triboelectric nanogenerators (TENGs) as a ferroelectric filler. It has been found through research that the inclusion of BTO particles in PDMS significantly enhanced energy harvest capacity. [5] In addition, NBT-BT is another lead free ferroelectric filler that promises to enhance the performance of these composites by providing superior dielectric and polarization characteristics. [6] Another possible ferroelectric filler that can be used to improve the performance of triboelectric nanogenerators (TENGs) is strontium-doped lanthanum cobalt oxide (LSCO). [7] Perovskite fillers, like vanadium-doped sodium niobate (V-$NaNbO_3$), can make things even better. [8]

Dual fillers and control of particle sizes will further make the system more efficient. This is because of the synergistic effect and effective particle dispersion. [9] Surface engineering is another method, where blocking of electron flow leads to charge accumulation at the interfaces. [10] Other materials, such as Bismuth Ferrite ($BiFeO_3$) and triple perovskites, are other higher potential materials for energy generation. [11,12]

The purpose of this work is to investigate the influence of 80NBT-20BT and $BaTiO_3$ particle size on the triboelectric and dielectric properties of 80NBT-20BT/PDMS and $BaTiO_3$/PDMS composites at a fixed filler concentration of 47wt.%.

The following tasks were formulated:

- To prepare 80NBT-20BT/PDMS and $BaTiO_3$/PDMS composite films (concentration: 0 and 47 wt.%), with different particle sizes (pure PDMS, five compositions for 80NBT-20BT/PDMS, and 3 compositions for $BaTiO_3$/PDMS) using the spin coating method.
- To investigate triboelectric properties of 80NBT-20BT/PDMS and $BaTiO_3$/PDMS films in contact with Al electrodes in vertical contact/separation TENG configuration.
- To investigate the dielectric properties of 80NBT-20BT/PDMS and $BaTiO_3$/PDMS films in the 100 Hz – 1 MHz frequency range at room temperature.

1. LITERATURE OVERVIEW

1.1 Fundamentals of Triboelectric Nanogenerators

Triboelectric nanogenerators (TENGs) are innovative instruments to transform mechanical energy into electricity by combining triboelectrification and electrostatic induction. It was invented by Wang's research group in 2012. [13] Unlike traditional electromagnetic generators, the structure of Triboelectric Nanogenerator (TENG) is completely separate from magnetic parts or inductive coils, owing to its ultra-light structure, despite being made of low density materials and inexpensive fabrication. [14] Every time the two different materials are brought into contact, one tends to gain electrons, the other tends to lose them. When they separate, an imbalance of charges is generated. [15]

1.1.1 Mechanism of triboelectrification

Triboelectrification is the scientific term used for contact electrification (CE). It is a process in which charges are produced when two materials come into contact, and electrons transfer from one material to the other. The separation of two layers by an external force results in a time-dependent voltage, which generates current in a device called a nanogenerator. Triboelectrification is universal; it occurs for all materials and phases of matter, including solid-to-solid, solid-to-liquid, and gas interactions. [16] As shown in Figure 1, the theoretical framework of TENG is an extension of Maxwell's equations, where mechanical energy is converted into electrical energy through the coupling of triboelectrification and electrostatic induction. [17] The use of triboelectrification and electrostatic induction for the generation of electricity was first presented by James Wimshurst in 1891 through the Wimshurst influence machine and further continued by Robert J. Van de Graff in 1929 with the high voltage electrostatic generator. While these early discoveries established the foundation for electrostatic energy conversion, the current Triboelectric Nanogenerator (TENG), announced in 2012, combines triboelectrification with electrostatic induction at the nanoscale to efficiently harvest ambient mechanical energy. [13,18]

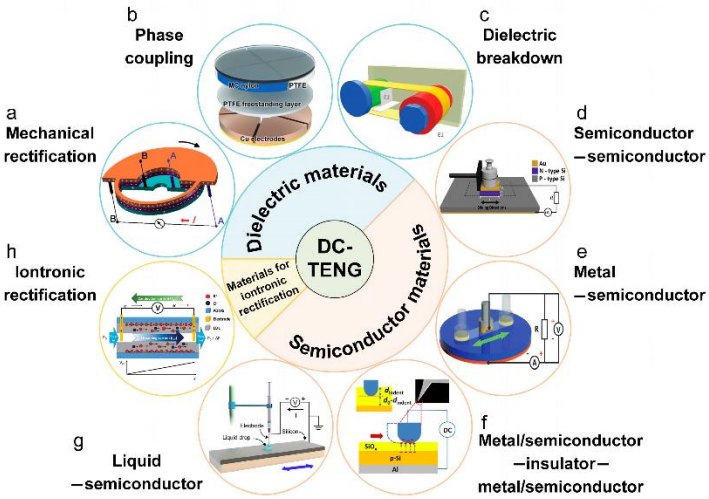

Figure 1. The theoretical basis of TENG based on expanded Maxwell's displacement current, showing how mechanical motion links with electrostatic induction. [17]

1.1.2 Fundamental Theory of Triboelectric Nanogenerators

According to the comprehensive theoretical framework provided by Wang [19], the fundamental physics of TENGs is rooted in Maxwell's displacement current, which explains how the coupling between contact electrification and electrostatic induction drives the electron flow in the external circuit. The expanded form of this current, which accounts for the polarization of the triboelectric charges, is expressed as:

$$J_D = \frac{\partial D}{\partial t} = \varepsilon \frac{\partial E}{\partial t} + \frac{\partial Ps}{\partial t} \qquad (1.1)$$

Where J_D represents the displacement current density, ε is the permittivity, E is the electric field, and Ps is the polarization created by the triboelectric surface charges.

TENGs provide continuous and stable high voltage output due to their periodic mechanical motion. The energy harvesting in TENGs depends on relative motion between triboelectric materials that creates enough movement of charge between the electrodes, which leads to an electric current that can be sent to a circuit outside. [20] Historically, it was observed that the material's charge is not fixed. This means that a material could become either positively or negatively charged depending on the material used to rub against it. [21] This relationship between voltage, charge, and distance is expressed below:

$$V = -\frac{1}{C(x)} Q + V_{oc}(x) \qquad (1.2)$$

Where the charge transferred between surfaces is represented by Q. The voltage created when the materials separate is defined as $V_{oc}(x)$, while the capacitance is distance dependent and defined as C(x).

The electrical output of a TENG is largely determined by its capacitance (C), which is usually represented as a parallel plate capacitor, particularly in the contact separation mode of operation. This relationship can be expressed in the form of an equation: [22]

$$C = \frac{\varepsilon_o \varepsilon_r A}{d} \qquad (1.3)$$

Where A refers to the effective area of contact, d refers to the distance between the triboelectric layers, ε_0 refers to the vacuum permittivity, and ε_r refers to the relative permittivity of the composite dielectric layer. The improvement of ε_r with the addition of several fillers to the polymer matrix of PDMS enhances dielectric properties, charge accumulation capacity, boosting the open circuit voltage (V_{oc} = Q/C), and the total amount of energy generated. As the relative permittivity increases, the internal impedance of the device reduces, which is essential to match the impedance of external loads and maximum power output. [15] In the case of TENGs, the Surface Charge Density (σ) is used to determine the total electric charge that is generated through contact electrification on the surface. The equation for surface charge density is expressed as:

$$\sigma = \frac{Q}{A} \qquad (1.4)$$

Where σ indicates surface charge density, Q is the transferred charge, and A is the contact area. Generally, a higher σ leads to higher output performance. When electrified surfaces are separated from each other, an electric field is created between them, causing a potential difference. A larger voltage is produced by increasing the distance (d) between two parallel plates. The electric field (E) in the gap is given by: [23]

$$E = \frac{\sigma}{\varepsilon_0} \qquad (1.5)$$

The resulting potential difference (V) between the two surfaces is directly proportional to the electric field and the separation distance, expressed in equation (1.6). It emphasizes that material level modifications are crucial for high performance output.

$$V = Ed \qquad (1.6)$$

Under open circuit conditions, where charges remain fixed on the surfaces as the materials separate, the induced electric field gives the maximum voltage while no current is flowing. The open circuit voltage (V_{oc}) can be expressed as:

$$V_{oc} = \frac{\sigma d}{\varepsilon_0} \qquad (1.7)$$

TENGs are flexible enough to use in many environments, which is why they are widely used in energy harvesting, high voltage sources, self powered systems, and other fields. A TENG's overall performance is strongly influenced by various parameters, such as the inherent properties of the materials used, the device architecture, and the operating environment.

1.1.3 Working modes of Triboelectric Nanogenerators

Triboelectric nanogenerators could be classified into four major categories depending on the electrode arrangement, structure, and working principles: Vertical contact separation mode, lateral sliding mode, single electrode mode, and freestanding triboelectric layer modes, as represented in Figure 2. [24] In the vertical contact separation mode (Figure 2a), the two triboelectric layers repeatedly come into and out of contact in a perpendicular direction. As the friction begins between two layers, the electrostatic charge begins to move to the surfaces. When the layers separate vertically, it creates a strong potential drop, forcing electrons to flow through an external circuit. The surface charge density increases with the increase in contact times and eventually stabilizes at a saturation level.

In the lateral sliding mode (Figure 2b), the layers slide against each other in a horizontal, parallel motion, resulting in transferring electrons through an external circuit. The single electrode mode (Figure 2c) is designed to harvest energy from freely moving objects without physical contact with the device. In this mode, only one electrode needs to be connected to the surface, and the charges will generate on the interface, inducing the external current. [25] The freestanding triboelectric layer mode (Figure 2d) combines aspects of vertical and lateral motion, using a pair of symmetric electrodes and electrostatic induction to efficiently capture mechanical energy. In our case, we are using a vertical contact separation type (Figure 2a). Combining contact electrification and electrostatic is the basic idea underlying how TENGs work. A charge transfer at the interface between

two materials with different triboelectric polarities leads to the buildup of surface charges. When these materials are separated later, an electric potential is created. This potential difference can drive electrons through an external circuit, creating an electric current.

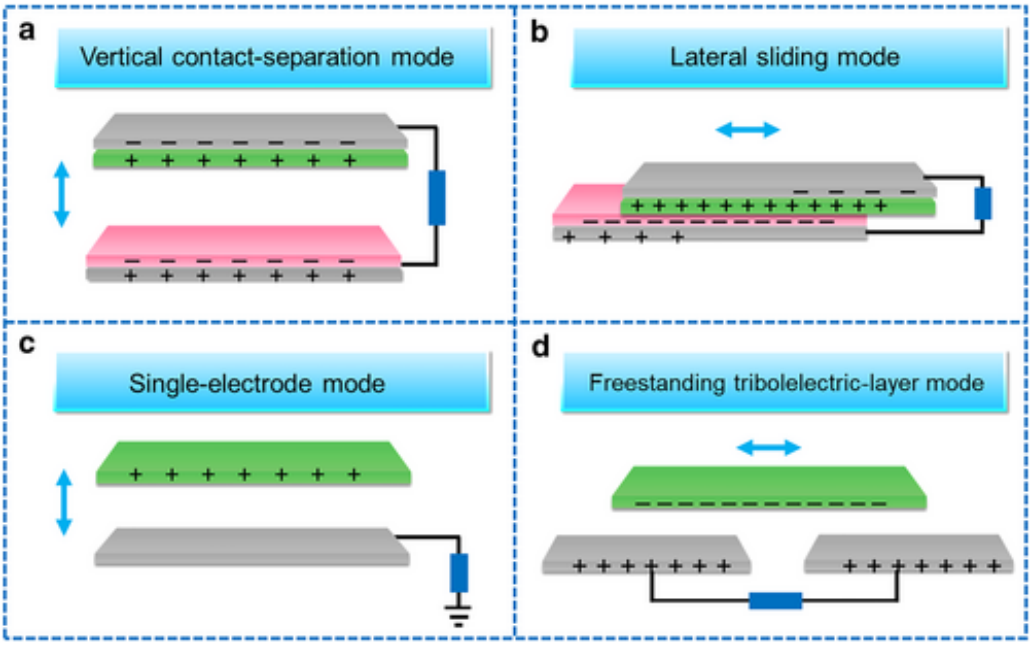

Figure 2. Four fundamental working modes of triboelectric nanogenerators (TENGs). **(a)** Vertical contact separation mode. **(b)** Lateral sliding mode. **(c)** Single electrode mode. **(d)** Freestanding triboelectric layer mode. [24]

1.1.4 Charge Transfer

Charge transfer in TENG is the fundamental step to convert mechanical energy into electrical energy. The primary working principle of TENGs is contact electrification and electrostatic induction. Physical contact between two materials with varying electron affinities will result in dynamic charge transfer, which can be described using capacitance characteristics in triboelectrification. [22] When the mechanical energy levels are high, charge transfer from the material's surface may occur.

The static charges on the surfaces cannot move through a circuit on their own. The charges need mechanical movement because it creates electron flow, which extends to their connected electrodes. [25] When two charged surfaces separate from each other or slide past each other, the balanced electric field gets shifted as the gap distance changes, and the two surfaces begin to move apart.

The charge transfer can be represented using the relationship between the surface charge density, displacement, and resulting voltage. [22] For a basic vertical contact separation TENG, the voltage V-Q-X relationship is generally derived from Gauss's Law:

$$Q_{sc} = \frac{A\sigma x(t)}{d_{eff} + x(t)} \quad (1.8)$$

In this equation Q_{sc} represents the amount of charge moving between electrodes, A is the contact area of both materials, x(t) is the gap distance between the two surfaces, and d_{eff} is the thickness of the dielectric layers.

1.1.5 Triboelectric Series

The triboelectric series is a classification of materials based on their ability to gain or lose electrons. The materials are listed in a way that when any two materials from the list are rubbed together, the material lower on the list tends to gain electrons and form a negative charge, while the one preceding in the list will lose electrons and create a positive charge. Electrons can have a stronger affinity for certain materials than others, depending on their relative position in the triboelectric series. Materials located in the center of the series are considered electrostatically stable, as they have a low tendency to either gain or lose electrons. Essentially, a material's rank in the triboelectric series is not fixed; it depends on its physical and chemical properties, such as surface roughness, adsorbents, and temperature of a material. [26] In the case of TENGs, the triboelectric series plays an important role in the choice of material, whereby different materials are placed in order according to their electron affinity. A material loses or gains electrons, depending on its place in this series, as illustrated in Figure 3. In general, the greater the difference between the two positive and negative materials, the higher the voltage produced by the TENG. [27]

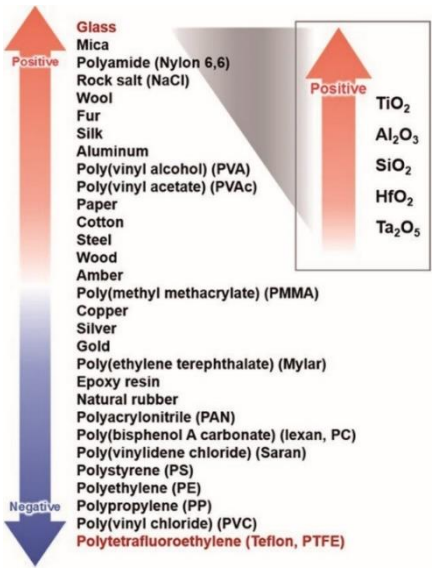

Figure 3. The triboelectric series shows the ranking of materials based on their electron affinity and charge polarity. [27]

The triboelectric series for different types of polymers is determined in a quantitative manner with regard to the triboelectric charge density (TECD) using a liquid metal as the reference, due to its softness and ability to change shape. It ensures the best possible surface contact with the material. The TECD is quantitatively measured in a glove box under controlled temperature, pressure, and humidity levels. Contacting and separating from the liquid metal keeps the contact pressure steady and improves the contact quality, resulting in more reliable results. [28]

The triboelectric Charge density is one of the key parameters in TENG, as it directly affects their performance. Several technologies have been developed to boost the triboelectric charge. A variety of methods have been developed to boost the triboelectric charge density, such as surface engineering, chemical functionalization, charge injection, and trapping mechanisms.

1.1.6 Maximum Power Transfer

Energy storage devices (ESDs) are known for their ability to deliver the maximum power output, which is largely influenced by their internal resistance. This maximum power output condition occurs when the value of the load resistance is equal to the internal resistance of the device, and can be expressed mathematically as:

$$I = \frac{V}{R_{L+r_{int}}} \tag{1.9}$$

Power delivered to the load is:

$$P_L = I^2 R_L = \left(\frac{V}{R_{L+r_{int}}}\right)^2 R_L \tag{1.10}$$

By differentiating this expression with respect to R_L and finding the maximum. The peak occurs when:

$$R_L = r_{int} \tag{1.11}$$

Applying this to the power equation (1.10) yields the maximum possible power: [19]

$$P_{max} = \left(\frac{V}{2R_L}\right)^2 = \frac{V^2}{4R_L} \quad (1.12)$$

Devices with low internal resistance, such as supercapacitors, can deliver high instantaneous power, making them suitable for applications that require rapid energy discharge. Conversely, batteries may exhibit increased internal resistance while discharging; therefore, they cannot provide maximum power output for a longer period of time. The main idea is that reducing internal resistance improves energy delivery efficiency in ESDs

Internal losses of energy in the device play another role in determining the efficiency of the transfer of energy. Internal losses of energy usually occur as heat energy due to internal resistance. For example, in the case of batteries, significant amounts of energy are lost as heat when discharging. Supercapacitors with their consistently low equivalent series resistance (ESR) values demonstrate superior performance in high power applications by minimizing these losses. It is important to know about these phenomena in order to choose an appropriate energy source. [29]

1.2 Composite materials

Composite materials are made up of a combination of various materials to form a new material with enhanced properties. As emphasized by Wang [19], the use of composite materials is an important step in fabricating TENGs to fill the existing gap between flexibility and efficiency. With the help of these materials, one can attain a level of efficiency that cannot be achieved with a single material.

1.2.1 Polymer Composites

Polymer composite is a combination of two or more polymers containing different properties, which allows combining features such as physicochemical, thermal, and separation properties as a resulting material at a specific proportion. Polymer composites can be produced in a wide range of shapes and sizes using various processing techniques, depending on the requirements of the application. Until now, polymer composites can be manufactured in diverse structures, including flat sheets, thin films, gel, sponge, nanofibers, and foam. [30] Polymeric materials have been extensively used in TENGs due to their broad triboelectric charge polarity range (from highly tribo-positive to highly tribo-negative), tunable chemical properties, and ease in shaping them into various forms such as thin films and micro/nanopatterns.

1.2.2 Perovskite-type materials

Perovskite-type materials are a key category of active fillers used to improve energy harvesting performance through piezoelectric effects. Perovskite materials are a whole family of compounds that share a similar crystal structure. The standard formula for perovskite oxides is ABO_3, in which A represents a bivalent or univalent metal, B represents a tetravalent atom, and O is usually oxygen anions that are positioned at the face center. Nearly every other element in the periodic table can occupy A or B sites in the perovskite structure, apart from naturally occurring liquids and gases. [31] These materials include well known examples like barium titanate ($BaTiO_3$) and various lead free alternatives, including vanadium-doped sodium niobate (V–$NaNbO_3$) and 0.80$Na_{0.5}$Bi0.5TiO3-0.20$BaTiO_3$ solid solution. The calculation of the electronic structure of these perovskite materials is essential as it helps to identify their band gaps. The electronic structure calculation of these perovskite materials is important as it helps determine their band gaps, the density of states, and the partial density of states.

1.2.2.1 Barium Titanate

As detailed by Wang [18], the incorporation of high permittivity ferroelectric fillers, such as Barium Titanate ($BaTiO_3$), is a strategic method to enhance the effective capacitance and surface charge density of the composite films, leading to a significant boost in the peak power density. Barium Titanate ($BaTiO_3$) is a material belonging to the perovskite oxide with high ferroelectricity and piezoelectricity characteristics, making it a good choice for nanogenerators. [32] Barium Titanate ($BaTiO_3$) can shift the positions of cations and anions in its crystal lattice under mechanical pressure, leading to macroscopic polarization. This polarization leads to the generation of surface charge, which is then used for power generation in piezoelectric nanogenerators (PENGs). [33] The phenomena, when combined with triboelectric and piezoelectric properties, make it perfect for use in self powered sensing and energy harvesting systems.

$BaTiO_3$ serves as a model system for understanding piezoelectricity in perovskite oxides. It is commonly referenced alongside lead zirconate titanate ($Pb(Zr,Ti)O_3$) as a key material for energy conversion applications. Because of its high dielectric constant and low loss characteristics, it has been used in applications such as multilayer ceramic capacitors (MLCs) and other high energy storage devices. One of the most significant ferroelectric ceramics is doped barium titanate, which is frequently utilized in semiconductors, PTC thermistors, and piezoelectric devices. [34] The perovskite unit cell of barium titanate, as represented by Figure 4, shows the cations at the corners, anions at the face centers, and the cation at the center of the oxygen octahedron.

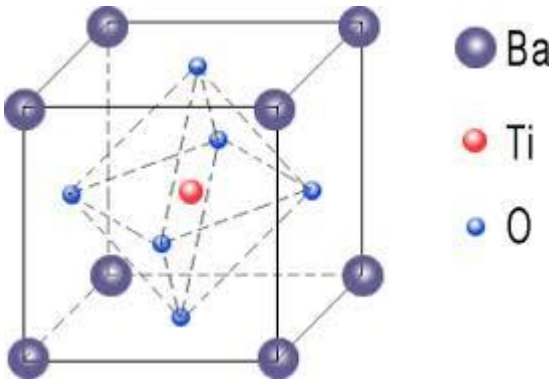

Figure 4. Perovskite unit cell of barium titanate. [34]

1.2.2.2 $0.80Na_{0.5}Bi0.5TiO_3$-$0.20BaTiO_3$ Solid Solution

The lead free ferroelectric ceramic Sodium Bismuth Titanate-Barium Titanate $0.80Na_{0.5}Bi_{0.5}TiO_3$-$0.20BaTiO_3$ (80NBT-20BT) has emerged as a particularly attractive prospect for improving the performance of PDMS based TENGs due to its remarkable piezoelectric and exceptionally high dielectric properties. When this material is used as a filler in a PDMS matrix, it improves the composite's electrical performance. The perovskite structure of NBT-BT allows polarization to develop inside the material when mechanical force is applied. As a result, the material can respond effectively to external stress and contribute to charge generation. Another advantage of NBT-BT is its stable behavior at room temperature. [35] The internal domain structure of NBT-BT/PDMS can easily adjust under stress, which supports continuous energy conversion. Due to these properties, NBT-BT/PDMS composites are considered suitable for use in flexible and efficient TENG devices. [36] The results for the ferroelectric behavior using P-E loops, along with the piezoelectric behavior through S-E plots, are presented in Figure 5. The corresponding values are for the series NBT–BT for variations in Na and Bi contents. This clearly depicts the effect of varying the content of Sodium (Na) and Bismuth (Bi) on the charge storage and mechanical deformation of the system. [37]

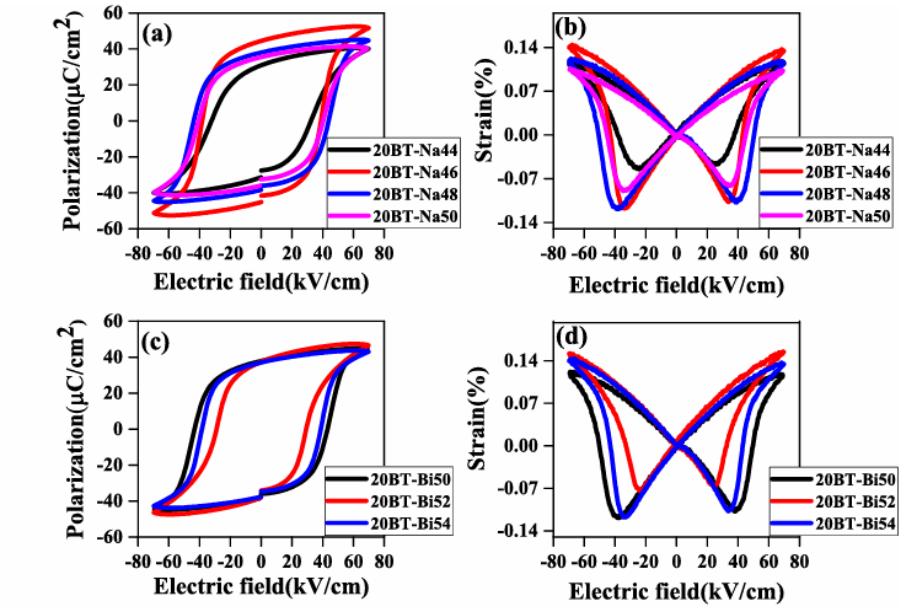

Figure 5. Ferroelectric (P-E) hysteresis loops and bipolar piezoelectric strain (S-E) curves for NBT–BT compositions with variable Na and Bi. [37]

1.2.3 Polymers-Based Composites for TENGs

TENGs, or triboelectric nanogenerators, are a new energy conversion technology. They will turn mechanical energies from the environment into electrical energy; polymers will be essential due to their tunable triboelectric characteristics and because they can vary from highly elastic to rigid depending on factors such as molecular structure, intermolecular forces, and crystallinity. [38]

Polydimethylsiloxane (PDMS) is one of the widely recognized tribo-negative polymers that is commonly used in TENGs because of its high electronegativity. Devices can tolerate bending, stretching, and deformation without cracking because of their extreme flexibility and optical transparency. [39] Moreover, the glass transition temperature of PDMS is low ($T_g \approx$ -125 °C), allowing it to maintain a rubber like, highly elastic state at room temperature. Its molecular structure contains nonpolar methyl (–CH_3) side groups that weaken intermolecular forces and reduce crystallinity, resulting in a soft and highly deformable material. [40] These intrinsic properties make PDMS an amorphous elastomer with excellent flexibility, which is particularly important for wearable and biomechanical triboelectric nanogenerators.

Thus, a highly efficient way to greatly increase the effective dielectric constant of the final composite is to strategically incorporate high-k fillers, such as Barium Titanate ($BaTiO_3$) and NBT–BT, into a PDMS matrix. The surface charge density produced during contact and separation rises significantly as a direct result of this improvement. The TENG device then produces a higher open

circuit voltage (V_{oc}) and a larger short circuit current (I_{sc}) as a result of the enhanced charge density. These output characteristics have a fundamental link with the device capacitance (C) and accumulated charge (Q):

$$V_{oc} = \frac{Q}{c} \tag{1.13}$$

$$I_{sc} = \frac{dq}{dt} \tag{1.14}$$

Where (q) is the instantaneous charge, and (t) is time. [19]

PDMS based polymer composites are used to improve TENG performance by enhancing electrical output. The inclusion of different types of filler materials and fabrication techniques has an impact on voltage, current, and power generation. The electrical performance of different PDMS based composite materials is listed below (Table 1), which shows how different additives influence electrical output.

Table 1. TENG's performance with PDMS based composites [30]

Composite Materials	**Process**	**Performance (Surface Area)**
PDMS/$SrTiO_3$	Spin-coating	130 V_{OC}, 1.4 μA, 90 μW
PDMS/BNNO-MWCNTs	Casting	300 V_{OC}, 8.5 μA, 7.03 W/m² (2 × 2 cm²)
PDMS/Silica	Blade Coating	254 V_{OC}, 20.4 μA, 4.37 W/m²
PDMS/AgNWs	Casting and rolling	33.4 V_{OC}, 4.5 mA, 0.162 W/m² (4 × 5 cm²)
PDMS (Agent ratio)	Spin-coating	54.3 V_{OC} (1 × 1 cm²)
PDMS/MXene	Spin-coating	453 V_{OC}, 131 μA

From this table, it is clear that due to its flexible and amorphous structure, PDMS can serve as an excellent host material for creating high performance energy harvesters.

1.2.4 Factors Affecting the Performance of TENGs

The performance of the TENG device depends on different interrelated parameters that affect its ability to convert mechanical energy into electric energy. The dissimilarity of electron affinities of the contacting materials causes charge generation, resulting in a larger surface charge density. The materials are often chosen based on their position within the triboelectric series, which is a classification of substances according to their electron donation or acceptance capabilities. Some of the parameters that affect the triboelectric performance of the materials include their surface characteristics, such as chemical composition, roughness, contamination, and environmental factors like moisture levels and humidity.

Another key issue is the effective contact surface area between triboelectric layers, which controls the charge density and improves the overall performance of TENGs. Figure 6 shows that the performance of triboelectric nanogenerators (TENGs) is governed by intrinsic material features such as polarity, dielectric constant, and mechanical durability, which determine charge generation and retention. [31]

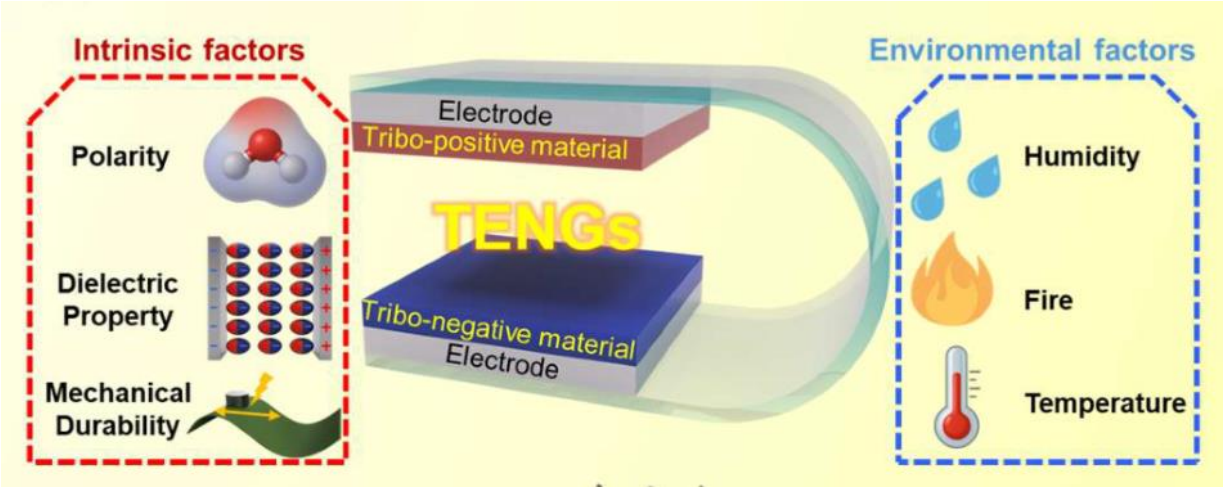

Figure 6. Factors affecting the performance of TENGs. [30]

1.2.5 Applications of Triboelectric Nanogenerators

The rapid development of various emerging types of polymeric materials for TENGs in recent years has demonstrated that the wide applications of TENGs come from their supremacy in harvesting low frequency energies, which outperforms electromagnetic generators.

TENG has many potential applications that can be categorized under:

- Motion energy harvesters transform mechanical energy from environmental sources such as human movement and wind into electrical energy to generate high voltage, relatively high power, and low current density.
- TENGs can be used to power high voltage machines like electrospinning, eliminating conventional sources of power in some cases. High voltage TENGs generate high electric fields that can affect the state of molecules, electrons, and ions within them, enabling applications like particle pollution filtration [41], substance movement control, substance analysis [42], and others.
- Self powered sensing systems are one of the cutting edge technologies of TENGS that power themselves using energy harvested from the environment, instead of external batteries. It offers excellent sensitivity, quick response times, and environmental friendliness, among other characteristics.
- TENGs are extremely sensitive to electron movement; they can act as probes at material interfaces (solid–solid or liquid–solid). [43] The intrinsic electron transfer capabilities of the TENG may have a completely different explanation for the charge transfer mechanism at this contact. This probing ability is useful in fields such as electrochemical catalysis, microfluidics, surface chemistry, and even biological systems, where understanding interfacial charge transfer is critical.

As illustrated in Figure 7, TENGs can be effectively configured in a variety of designs and operating modes to provide autonomous power solutions for systems operating in a variety of settings, ranging from human bodies to the oceans. [44]

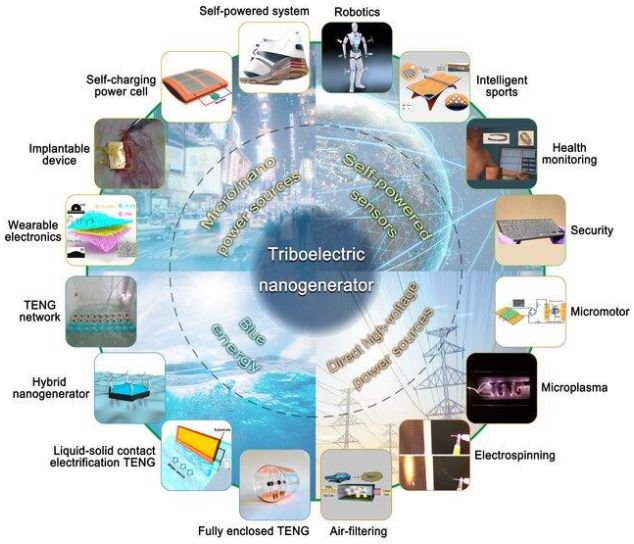

Figure 7. Four major application domains of TENGs. [44]

2. MATERIALS AND METHODS

2.1 Materials and Composite Preparation

Two different types of ferroelectric particles were considered: and the first material, sodium bismuth titanate–barium titanate ($0.8Na_{0.5}Bi_{0.5}TiO_3$–$0.2BaTiO_3$ or 80NBT-20BT), was meticulously synthesized using a conventional solid state reaction method. [6] This synthesis began with the accurate mixing of precursor powders, which included titanium dioxide, sodium carbonate, bismuth oxide, and barium carbonate. The mixture was then subsequently milled in isopropyl alcohol (IPA) for 24 hours at 150 RPM (revolutions per minute) with a Planetary mono mill PULVERISETTE 6 (Fritsch, Germany) to guarantee uniform dispersion. Subsequent calcination at 900 °C for 4 hours produced the 80NBT-20BT powder designated as 1-NBT-BT. To reduce particle size, the 1-NBT-BT powder was subjected to a second planetary milling phase for an additional 24 hours under the same conditions. This method successfully produced the 2-NBT-BT powder. This technique was repeated for the remaining samples: the 3-NBT-BT powder was prepared by milling the preceding 1-NBT-BT sample for 72 hours. Further increasing the milling duration to 152 hours resulted in the production of the 4-NBT-BT powder. Finally, the 5-NBT-BT powder was produced by milling the 1-NBT-BT material for 272 hours. The specific milling durations for all samples are summarized in Table 2. This mechanical process is commonly referred to as planetary ball milling.

Table 2. 80NBT-20BT powder labeling and corresponding planetary ball milling time

Powder Label	Total Milling Time (h)
1-NBT-BT	0
2-NBT-BT	24
3-NBT-BT	72
4-NBT-BT	152
5-NBT-BT	272

The second material is a commercially available Barium Titanate ($BaTiO_3$) nano powder. Three different $BaTiO_3$ variants were selected to investigate the influence of filler size on the PDMS, denoted by 1-$BaTiO_3$, 2-$BaTiO_3$, and 3-$BaTiO_3$. These samples had varying particle sizes, which were 700 nm for sample 1-$BaTiO_3$ (sourced from *Sigma-Aldrich*), 300 nm for sample 2-$BaTiO_3$ (US Research Nanomaterials, Inc.), and 80 nm for sample 3-$BaTiO_3$ (US Research Nanomaterials, Inc.). [46].

For composite preparation, the polymer matrix, namely Polydimethylsiloxane (PDMS), specifically Sylgard 184 silicone elastomer, was used. This polymer material was selected as the base for the energy harvesting layers due to its great mechanical flexibility, high optical transparency, and chemical stability. Sylgard 184 consists of two parts: a silicone base and a curing agent (hardener) that are combined in a typical 10:1 weight ratio to provide effective cross-linking. Due to the hydrophobic nature and low surface energy of this material, it becomes possible to efficiently create and maintain surface charges, making it ideal for triboelectric applications. [47] The important physical and electrical characteristics of the PDMS matrix are shown in Table 3.

Table 3. Physical and Electrical Properties of PDMS

Property	**Value/Specifications**
Material Name	Sylgard 184
Cured Density	0.97 g/cm³
Dielectric Constant (at 100 Hz)	2.65 – 2.70
Dielectric Strength	24 kV/mm
Refractive Index	1.41
Tensile Strength	6.7 MPa
Viscosity (Mixed)	3500 mPa·s
Thermal Stability	-45°C to 200°C

A multi-step procedure is required to prepare PDMS based composite films with ceramic particles for the triboelectric nanogenerators design purpose. The same process was followed for both 80NBT-20BT and $BaTiO_3$ fillers as represented in Figure 8. To guarantee uniform dispersion and break down agglomerates, the proper amount of ceramic particles (either 80NBT-20BT or $BaTiO_3$) is first dispersed in isopropyl alcohol using a 1.5-hour sonication process. After adding the necessary uncured PDMS to the CERAMIC/IPA solution, the particles are sonicated for an additional 3 hours to ensure strong integration into the polymer matrix. The CERAMIC/IPA/PDMS solution is then heated on a hot plate magnetic stirrer to 80°C for several hours to eliminate the IPA solvent. Constant stirring ensures complete evaporation and prevents particle settling. After the IPA is removed and a viscous CERAMIC/PDMS remains, the PDMS curing agent is added at a 1:10 ratio to the PDMS. To guarantee homogeneity without adding too many air bubbles, the mixture is gently stirred by hand for 10 minutes. The CERAMIC/PDMS/hardener slurry is now prepared for film decomposition. A Polos Spin 150i Spin Coater is used to precisely apply the composite film onto a 2.5 × 2.5 cm^2 ITO-PET (indium tin oxide coated polyethylene terephthalate) substrate at 800 rpm for 120 seconds. This process guarantees a thin, consistent, and flawless coating. Finally, to enable full PDMS cross linking

and produce a mechanically and electrically stable composite that is essential for long lasting TENG performance, the spin-coated film is thermally cured for 3 hours at 110°C. The amount of filler concentration was 47 wt.% for all 80NBT-20BT/PDMS and $BaTiO_3$/PDMS composites. The thickness of each composite film was calculated using a screw gauge. Table 4 presents the thickness values for pure PDMS, PDMS/80NBT-20BT, and PDMS/$BaTiO_3$ composite films.

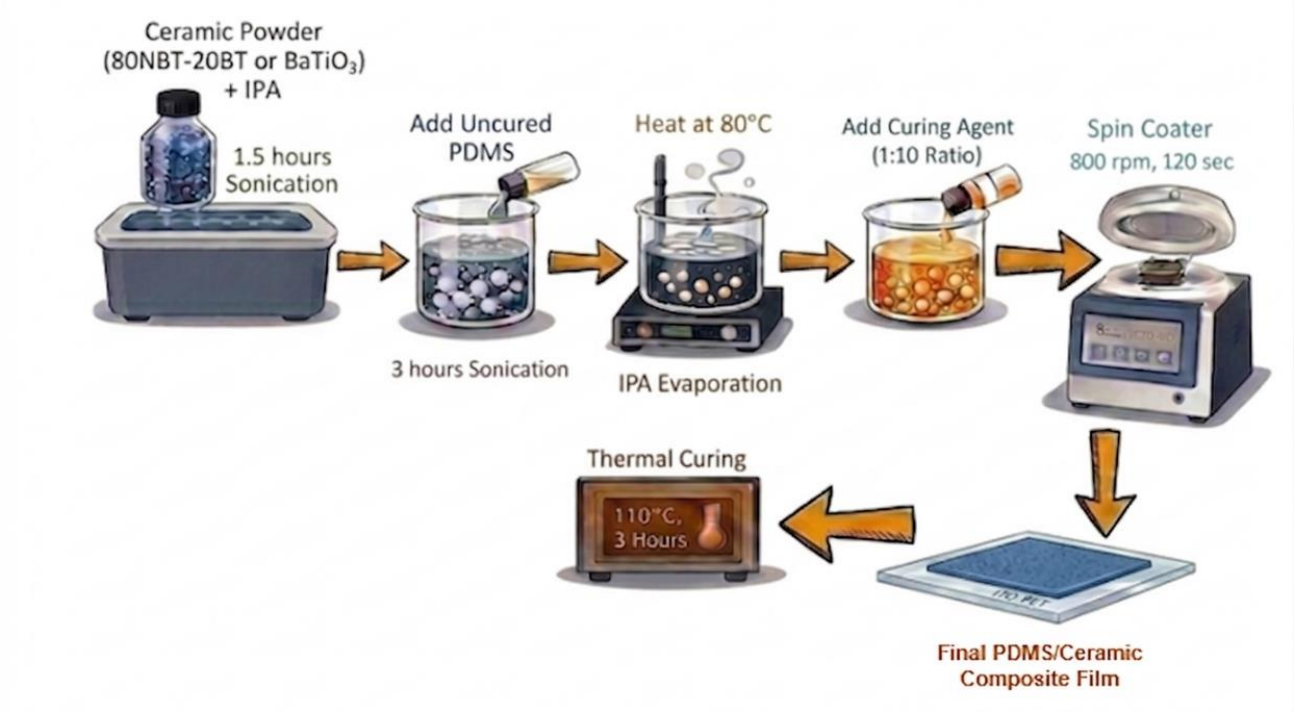

Figure 8. Schematic Diagram of the preparation process for PDMS-based composite films with ceramic particles

Table 4. Thickness of pure PDMS, 80NBT-20BT/PDMS, and $BaTiO_3$/PDMS composite films.

Sample Label	Thickness (mm)
Pure PDMS	0.07
1-NBT-BT/PDMS	0.07
2-NBT-BT/PDMS	0.09
3-NBT-BT/PDMS	0.08
4-NBT-BT/PDMS	0.08
5-NBT-BT/PDMS	0.09
1-$BaTiO_3$/PDMS	0.09
2-$BaTiO_3$/PDMS	0.08
3-$BaTiO_3$/PDMS	0.14

2.2 Measurement Methodology

The experimental setup to measure the triboelectric nanogenerator output involved applying a repeated vertical compression force (F) of approximately 20 N at a frequency of 1 Hz. A circular tip with a surface area of 2 cm^2, designed that is used to make direct contact with the sample and smaller than the sample's area, was prepared using a 3D printer and attached to the moving part of the pushing electromagnet. Pushing the electromagnet is the source of vertical periodic blows. As shown in Figure 9, the setup was configured in two variations of the Contact Separator system: (a) for measuring the triboelectric performance, and (b) for conducting the dielectric measurements.

In the TENGs under consideration, pure PDMS and various ferroelectric filled composite films, specifically 80NBT-20BT/PDMS (1-5) and $BaTiO_3$/PDMS (1-3), along with aluminum (Al) foil, served as the friction layers. PDMS and aluminum (Al) were selected because they are at the opposite ends of triboelectric series, as mentioned in Figure 3. This is due to their different electron affinities: aluminum (Al) can easily donate electrons, while PDMS easily accepts them; the pair creates a much higher electrical charge and higher output. The Al foil simultaneously functioned as the top contact, while ITO-coated PET (ITO-PET) was used as the bottom contact, onto which the PDMS based layers were deposited, as shown in Figure 10. The effective contact area of the Al foil was 2 cm^2, as it was attached to a circular tip. Here, triboelectrification occurred between polymers (pure PDMS, 80NBT-20BT/PDMS, and $BaTiO_3$/PDMS) and aluminum (Al) foil.

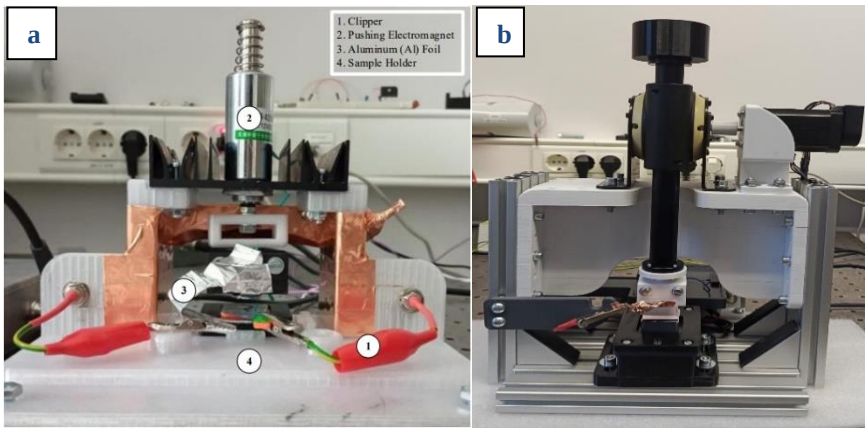

Figure 9. Variation of the Contact Separator systems **(a)** setup for measuring triboelectric output parameters showing: (1) Clipper, (2) Pushing Electromagnet, (3) Aluminum (Al) Foil, and (4) Sample Holder; **(b)** Setup for capacitance and dielectric permittivity characterization.

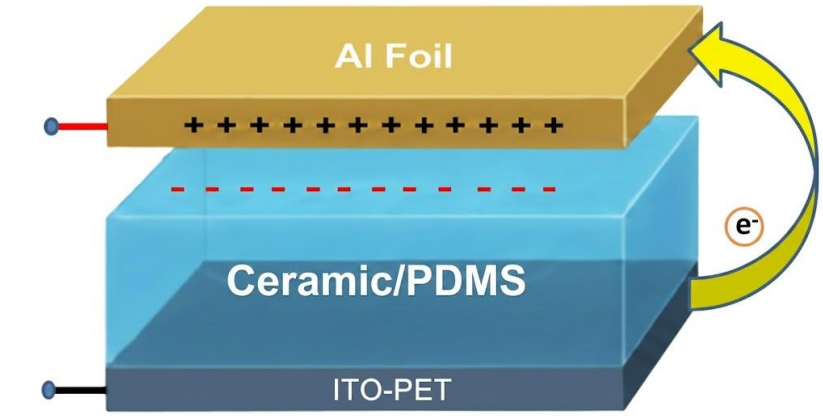

Figure 10. Schematic illustration of the TENG device structure

The electrical performance of the TENGs was evaluated by measuring the open circuit voltage (V_{oc}), short circuit current (I_{sc}), voltage (V), and current (I) under varying resistive loads. As shown in Figure 11(a, b), the V_{oc} and I_{sc} were measured by connecting the TENG terminals directly to the measurement instrumentation to capture the maximum potential and charge flow, respectively. For load dependent measurements, a variable resistor was integrated into the circuit, as shown in Figure 11(c, d), to evaluate the performance of the TENG nanogenerator across 21 distinct load resistances (100 kΩ - 500 GΩ).

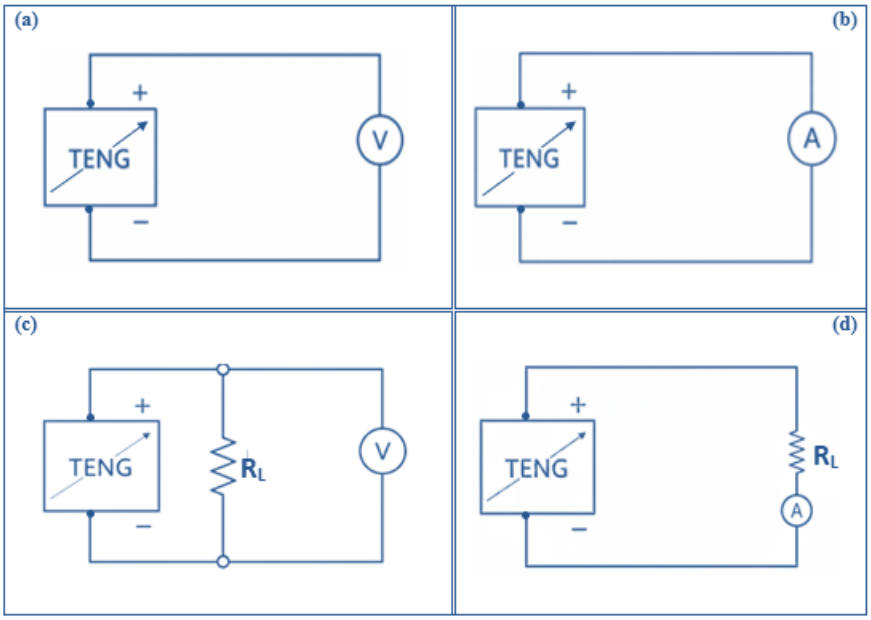

Figure 11. Illustrations of electrical circuits connected to the TENG and used for measuring the following triboelectric output parameters: **(a)** open circuit voltage (V_{oc}), **(b)** short circuit current (I_{sc}), **(c)** output voltage (V), and **(d)** output current (I) through a variable load resistor (R_L).

The triboelectric measurements were performed using electrical circuits connected to the TENG, including a load resistor to measure voltage and current across different resistances, and appropriate instrumentation, such as a Handy scope HS3 USB oscilloscope and a Keithley 6514 electrometer. These measurements included 12 low resistance loads under 20% symmetry, followed by 12 high resistance loads assessed with 50% symmetry.

The capacitance of the 80NBT-20BT/PDMS and $BaTiO_3$/PDMS composites was measured at room temperature. This characterization was performed using a Solartron Modulable XM MTS system connected to the Contact Separator device. The electrical output was measured systematically with different forces (1N, 5 N, 10 N, 15 N, and 20 N) to investigate the enhancement in charge density and the performance of TENG with the increase of pressure. For both samples, the measurements were carried out over a frequency range of 100 Hz to 1 MHz. By using the same experimental setup, dielectric permittivity was also measured for 80NBT-20BT/PDMS and $BaTiO_3$/PDMS composites. These measurements are important for understanding the material's ability to store electrical energy and its triboelectric and dielectric properties, which can influence the overall performance and energy conversion efficiency of the nanogenerator.

Particle size of the 80NBT-20BT powders and distribution of 80NBT-20BT inside PDMS composites were qualitatively evaluated by scanning electron microscopy (SEM) using a Helios NanoLab 650 microscope (Thermofisher Scientific, Hillsboro, USA).

3. RESULTS AND DISCUSSIONS

3.1 Scanning Electron Microscopy Characterization of 80NBT-20BT and $BaTiO_3$ Powders

A Scanning Electron Microscopy (SEM) is a popular characterization technique that provides detailed information by scanning the surface with a focused beam of high-energy electrons. about the surface morphology and microstructural features of materials. The interaction between the electron beam and the sample surface provides signals that are used to create high-resolution pictures, allowing for precise measurements of particle shape, size, agglomeration, and surface texture. SEM is widely used for studying composite materials, where changes in dispersion and clustering can significantly influence material properties.

In this work, SEM was widely used to examine the microstructural characteristics of five 80NBT-20BT powders, as shown in Figure 12(a-e). The particle size analysis was limited to a qualitative assessment. The qualitative evaluation of the morphology of 80NBT-20BT powder after ball milling treatments of different durations yields the following observations. The powders contain two particle fractions with different size distributions, a larger fraction at approximately 300 ± 100 nm and a smaller fraction at approximately 100 ± 50 nm, as clearly shown in Figure 12(a). To highlight the distribution of these multiple fractions, Figure 12(a) shows two red circles: the larger one indicates a representative portion of the large partial fraction, while the smaller circle shows the small fraction. The smaller particles tend to form agglomerates with dimensions comparable to those of the large fraction, which leads to dense packing and pronounced clustering at lower processing levels.

With increased ball milling time, a systematic reduction in the larger fraction and a corresponding increase in the smaller fraction are observed. Specifically, the mechanical impact of ball milling causes larger particles to fracture, reducing the number of large fractions and increasing the proportion of smaller particles as the milling duration increases. This evaluation is accompanied by a clear breakdown of agglomerates and a transition toward a more uniform distribution, as shown in Figures 12(b-d). At the highest milling time, Figure 12(e), the powders display the smallest apparent particle size, minimal agglomeration, highest level of dispersion, characterized by well separated particles. Overall, the SEM analysis demonstrates a clear evolution in morphology across the powders, with a progressive reduction in agglomeration and particle size from 1-NBT-BT to 5-NBT-BT, highlighting systematic microstructural changes within the 80NBT-20BT powder system as ball milling time increases.

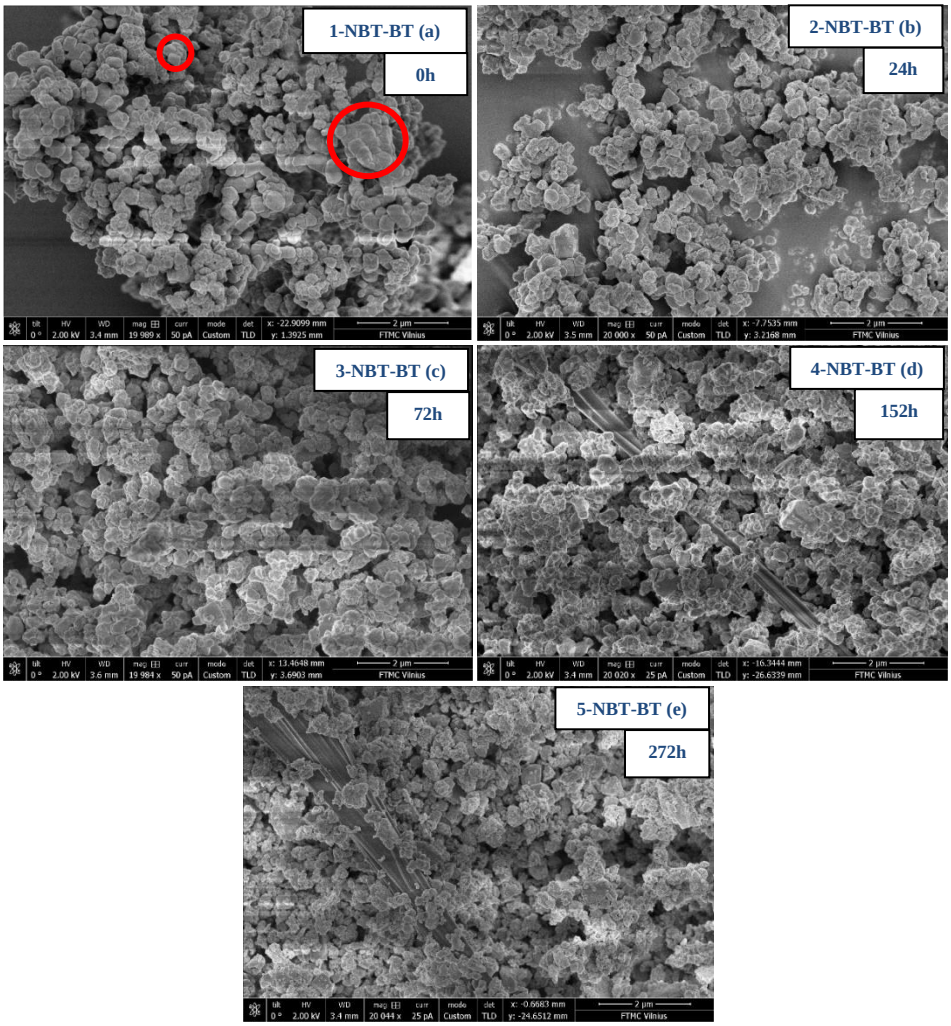

Figure 12. SEM micrographs of 80NBT-20BT powders: **(a)** 1-NBT-BT, **(b)** 2-NBT-BT, **(c)** 3-NBT-BT, **(d)** 4-NBT-BT, and **(e)** 5-NBT-BT.

The morphology and surface structure of the synthetic $BaTiO_3$ fillers (1-3) were also investigated, and the scanning electron microscopy (SEM) images of these ceramic fillers are shown in Figures 13(a–c)). Comparing these micrographs, it is clear that the average particle size decreases from 1-$BaTiO_3$ to 3-$BaTiO_3$. Figure 13a demonstrates that the 1-$BaTiO_3$ sample has the highest particle size of 700 nm, with grains that appear extremely thick and solid. In Figure 13b, the 2-$BaTiO_3$ particles have reduced in size to 300 nm, and grains become more defined but remain medium-sized. Finally, in Figure 13c, at around 80nm, the 3-$BaTiO_3$ sample has a totally different texture; the particles are particularly fine, microscopic, and more equally distributed. This shift is significant because the fine texture of 3-$BaTiO_3$ produces a significantly smoother mixture when combined with the PDMS polymer.

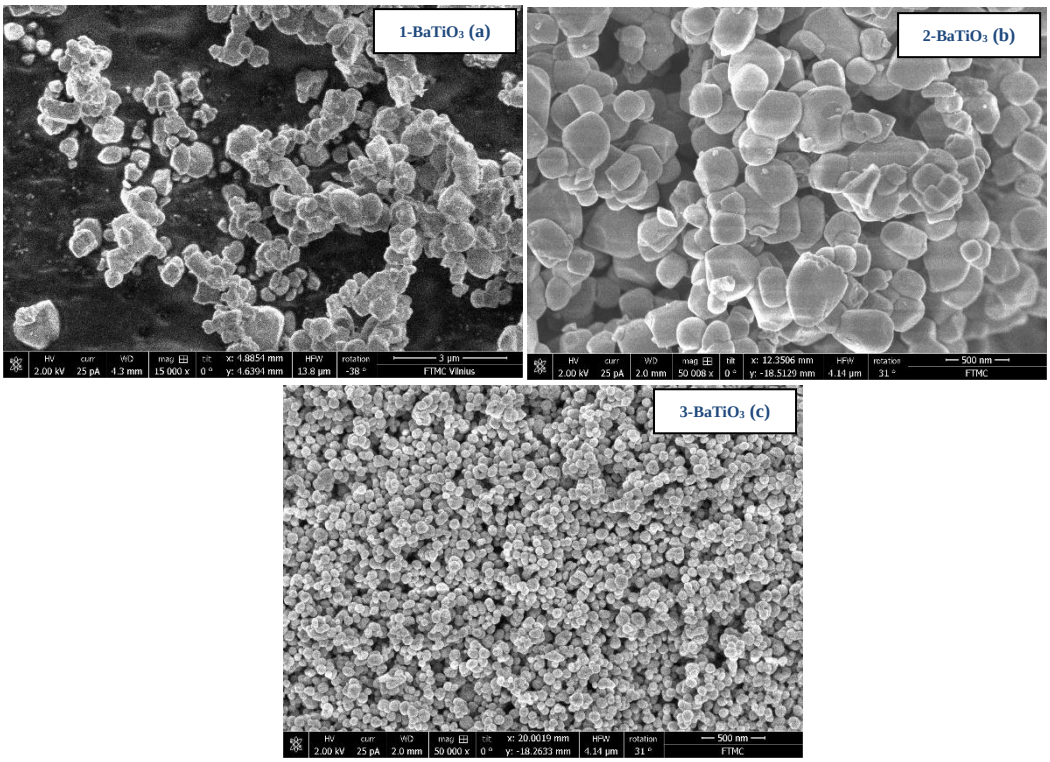

Figure 13. SEM micrographs of $BaTiO_3$ powders: **(a)** 1-$BaTiO_3$, **(b)** 2-$BaTiO_3$, **(c)** 3-$BaTiO_3$

3.2 Scanning Electron Microscopy Characterization of 80NBT-20BT/PDMS composites

The morphological and structural evolution of NBT-BT particles mixed with PDMS was also examined by SEM analysis. The SEM images, as seen in Figure 14(a-c), show that the 80NBT-20BT particles are distributed uniformly within the PDMS polymer matrix. This uniform distribution is important because it ensures the material works consistently and hence enhances the overall performance of the TENG. The bright white spots are the dense 80NBT-20BT particles, while the dark gray background represents the PDMS matrix.

The distribution of the particles in each sample differs significantly. While in both 1-NBT-BT/PDMS (Figure 14(a)) and 5-NBT-BT/PDMS (Figure 14(c)) films, there is an extremely smooth and homogeneous distribution of the particles, in the case of the 3-NBT-BT/PDMS (Figure 14(b)) sample, the particles form large agglomerates. Despite the equal fabrication method of all samples, it seems that in the case of certain samples, the particles re-agglomerated, which means that they bonded with one another. There are several reasons for such behavior: firstly, it may be associated with capillary forces that lead to aggregation of the particles during the drying process of the film [48]; secondly, ball milling results in the increased activity of particles, which leads to their re-aggregation [49]. Even after ultrasonic treatment, the mechanisms of behavior of the particles in the polymer are rather complicated and require further study [50].

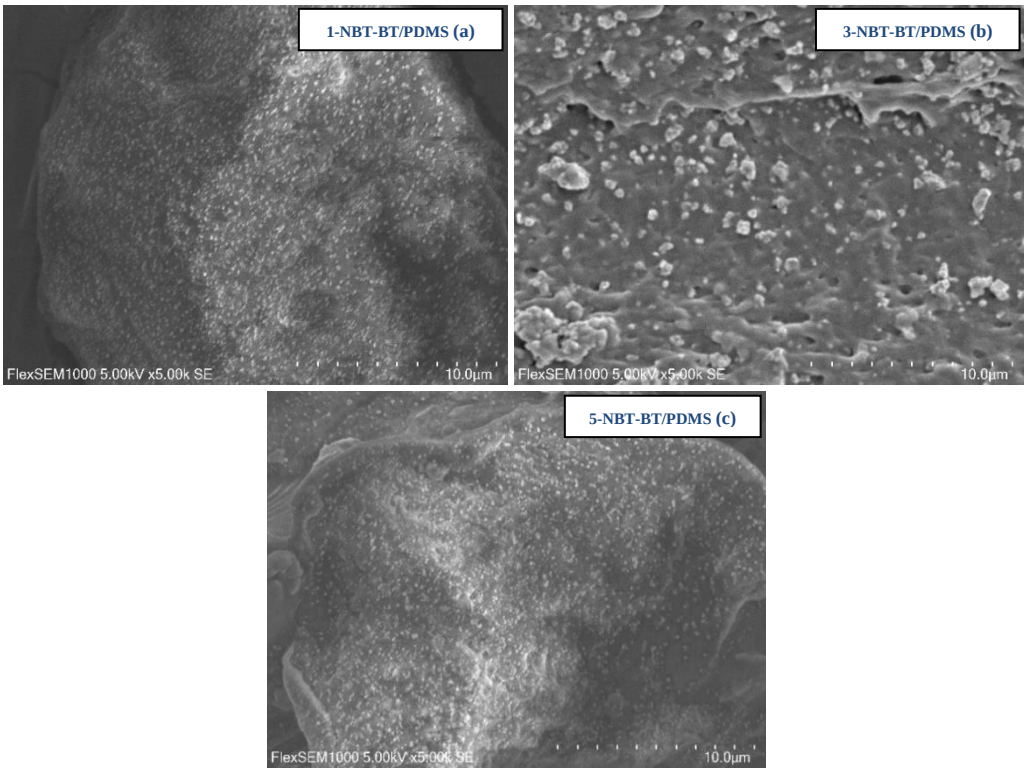

Figure 14. SEM micrographs of 80NBT-20BT/PDMS powders: **(a)** 1-NBT-BT/PDMS, **(b)** 3-NBT-BT/PDMS, and **(c)** 5-NBT-BT/PDMS.

3.3 Voltage Open Circuit and Short Circuit Current

Let's consider a 1 Hz contact separation cycle in detail. Figure 15 presents a detailed single pulse characterization of the triboelectric nanogenerator, simultaneously showing the short circuit current (I_{sc}) and open circuit voltage (V_{oc}) waveforms over a relative time of one second. Figure 15(a) illustrates the current, displaying a characteristic biphasic pulse. As the device is compressed or enters contact mode (indicated by "Contact" in the voltage plot), the current exhibits a sharp positive peak (approximately 0.9 µA), indicating forward charge transfer. Furthermore, when it comes to the release or separation stage, it shows a negative peak (approximately -0.15 µA), due to the reverse flow of charges. Figure 15(b) represents the behavior of the open circuit voltage. It starts at approximately 95V, then drops to around 45V during the active generation phase (contact). Once separation occurs, the voltage returns to its high state**.**

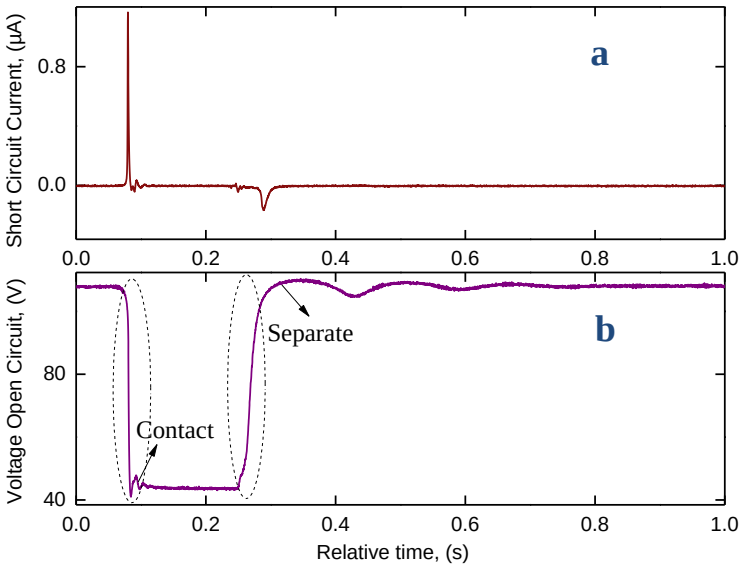

Figure 15. Enlargement of one cycle **(a)** Short Circuit Current I_{sc} (top) and **(b)** Open Circuit Voltage V_{oc} (bottom) pulses for pure PDMS sample

Figure 16(a) illustrates the dynamic open circuit voltage (five pulses) response of vertical contact separation mode triboelectric nanogenerators (TENGs), during repeated cycles of contact-separation, comparing pure PDMS (red), 1-NBT-BT/PDMS (black), 2-NBT-BT/PDMS (blue), 3-NBT-BT/PDMS (green), 4-NBT-BT/PDMS (orange), and 5-NBT-BT/PDMS (purple). Between the contact and separation positions, pure PDMS exhibits the lowest voltage output difference, approximately 67V. When 80NBT-20BT fillers are added, the open circuit voltage increases. The open-circuit voltages are 74 V, 98 V, 160 V, 146 V, and 118 V for 1-NBT-BT/PDMS, 2-NBT-BT/PDMS, 3-NBT-BT/PDMS, 4-NBT-BT/PDMS, and 5-NBT-BT/PDMS, respectively. The voltage peaks at 3-NBT-BT/PDMS and slightly decreases for the samples with longer milling times, such as 4-NBT-BT/PDMS and 5-NBT-BT/PDMS. Overall, the graph clearly shows that adding 80NBT-20BT to PDMS significantly increases the open circuit voltage of TENGs, with 3-NBT-BT/PDMS exhibiting the highest performance.

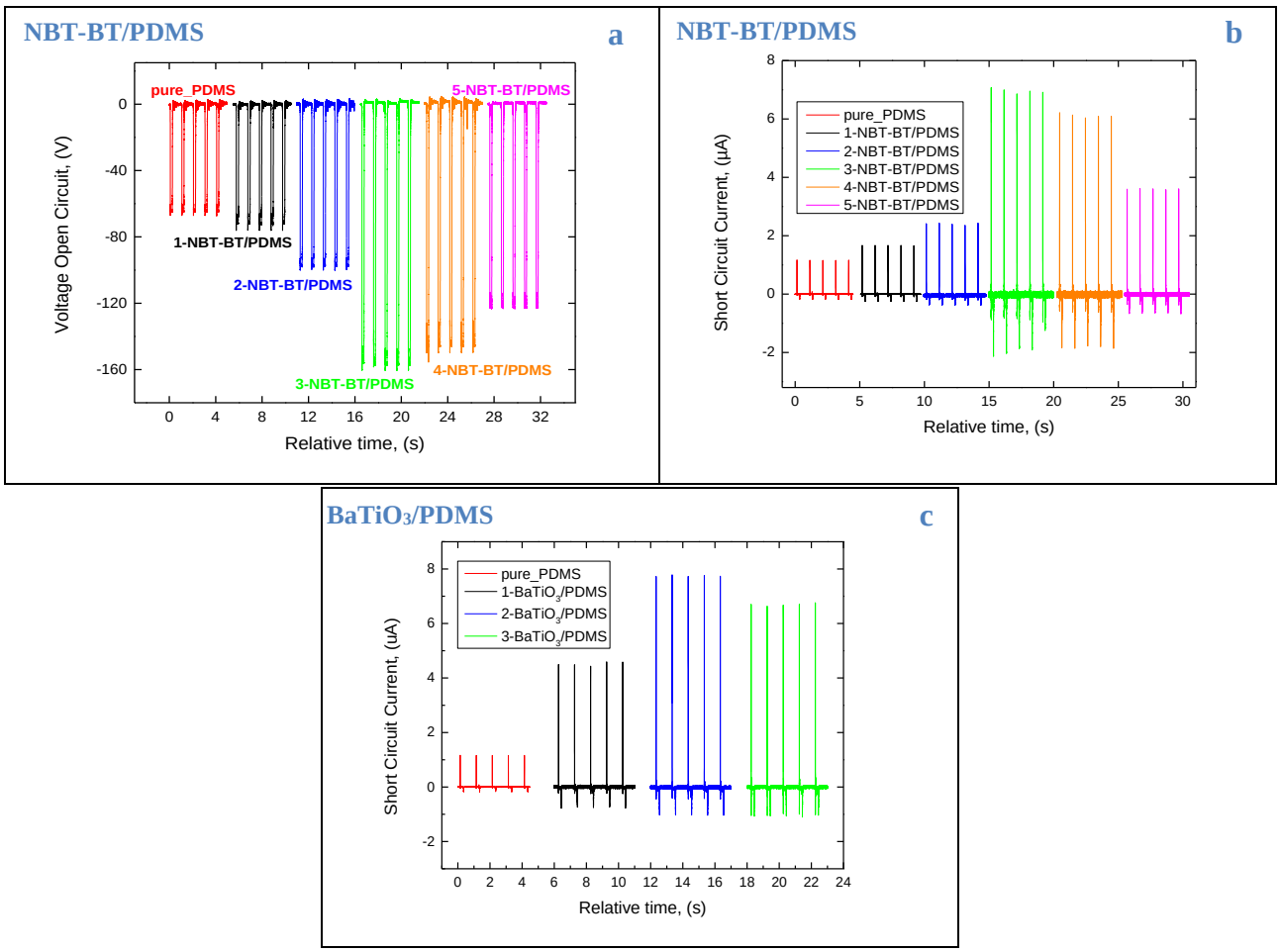

Figure 16. (a) Open Circuit Voltage V_{oc}, generated from 80NBT-20BT/PDMS-based TENGs (all compositions: pure PDMS, 1-5 NBT-BT/PDMS), **(b)** Short Circuit Current I_{sc} generated from 80NBT-20BT/PDMS-based TENGs (all compositions: pure PDMS, 1-5 NBT-BT/PDMS), and **(c)** Short Circuit Current I_{sc}, generated from $BaTiO_3$/PDMS-based TENGs (all compositions: pure PDMS, 1-3 $BaTiO_3$/PDMS) by applying a repeated vertical compression force of approximately 20 N at a contact–separation frequency of 1 Hz

The short circuit current (five pulses) output for triboelectric nanogenerators (TENGs) is displayed in Figure 16(b). It compares pure PDMS (red), 1-NBT-BT/PDMS (black), 2-NBT-BT/PDMS (blue), 3-NBT-BT/PDMS (green), 4-NBT-BT/PDMS (orange), and 5-NBT-BT/PDMS (purple). The pure PDMS device shows current pulses peaking at approximately 1.2 µA. In contrast, the 1-NBT-BT/PDMS composite reaches 1.8µA, and the 2-NBT-BT/PDMS composite achieves approximately 2.2µA. The 3-NBT-BT/PDMS composite shows a significant increase, reaching a maximum of 7.2 µA. For the remaining samples, the output subsequently decreases, with the 4-NBT-BT/PDMS composite reaching 6.3 µA and the 5-NBT-BT/PDMS composite decreasing to 3.8 µA. These distinct peak current values indicate that the 3-NBT-BT/PDMS delivers the highest current output.

Figure 16(c) presents the performance of short circuit current for the triboelectric nanogenerators (TENGs) devices where $BaTiO_3$ fillers are incorporated into the PDMS matrix. In this graph, three different samples were considered, including 1-$BaTiO_3$/PDMS (black), 2-$BaTiO_3$/PDMS (blue), and 3-$BaTiO_3$/PDMS (green). Pure PDMS has a very low value of current, i.e., 1.2 µA, as shown in Figure 16(c). However, when $BaTiO_3$ fillers are added to the PDMS matrix at a fixed concentration, there is an improvement in the generation of electrical current. The current increases to values of 4.1 µA (1-$BaTiO_3$/PDMS), 7.7 µA (2-$BaTiO_3$/PDMS), and 6.5 µA (3-$BaTiO_3$/PDMS). Among all the samples, the 2-$BaTiO_3$/PDMS sample performs the best, as it generates the highest current pulses.

In comparing the data obtained for both graphs, it can be clearly seen that $BaTiO_3$ provides better performance in terms of current generation. The highest value achieved by the 80NBT-20BT material was 7.2 µA, while in the case of $BaTiO_3$, we can see even higher results of 7.7 µA. This shows that incorporating $BaTiO_3$ into PDMS is a great way to increase the current flow and enhance the overall energy output of the nanogenerator.

3.4 Surface Charge Density

Surface charge density is known as the total amount of charge (q) dispersed over a specific area (A). The surface charge density (σ) is one of the important parameters that is used to evaluate the efficiency of a triboelectric nanogenerator (TENG). The σ value is obtained by integrating the short circuit current (I_{sc}) over a certain period of time, and then dividing it by the triboelectric nanogenerator's effective contact area (A).

The surface charge density can be computed using the given formula:

$$\sigma = \frac{Q}{A} \tag{3.1}$$

where,

$$Q = \int I_{sc}(t)\, dt \tag{3.2}$$

So,

$$\sigma = \frac{1}{A}\int I_{sc}(t)\,dt \tag{3.3}$$

Here, $I_{sc}(t)$ represents the instantaneous short circuit current, t is time, and A is the active contact area of the triboelectric material. In fact, the surface charge density can be determined by integrating the total area of each current pulse (positive or negative) created during the charge transfer process. The result obtained helps to find the electrical charge produced per unit area.

Figure 17 presents the surface charge density, a key indicator of triboelectric performance, for pure PDMS and 80NBT-20BT/PDMS calculated from the positive and negative I_{sc} peak (nC/cm^2). Pure PDMS exhibited positive/negative surface charge densities of 1.1/ -1.0 nC/cm^2. The incorporation of 80NBT-20BT fillers led to an initial improvement, with the 1-NBT-BT/PDMS increased these values to 1.6/-1.2 nC/cm^2, and 2-NBT-BT/PDMS yielding higher values of 1.8/-1.9 nC/cm^2. A significant performance surge was observed with 3-NBT-BT/PDMS, which achieved the maximum charge density of 7.1/-7.2 nC/cm^2. However, further filler modification resulted in a downward trend, with 4-NBT-BT/PDMS showing a reduced density of 5.5/-5.4 nC/cm^2 and 5-NBT-BT/PDMS dropping to 2.8/-3.0 nC/cm^2. This overall trend suggests that while NBT-BT incorporation significantly enhances the charge transfer and triboelectric performance, there is an optimal composition (3-NBT-BT) beyond which the performance begins to decrease.

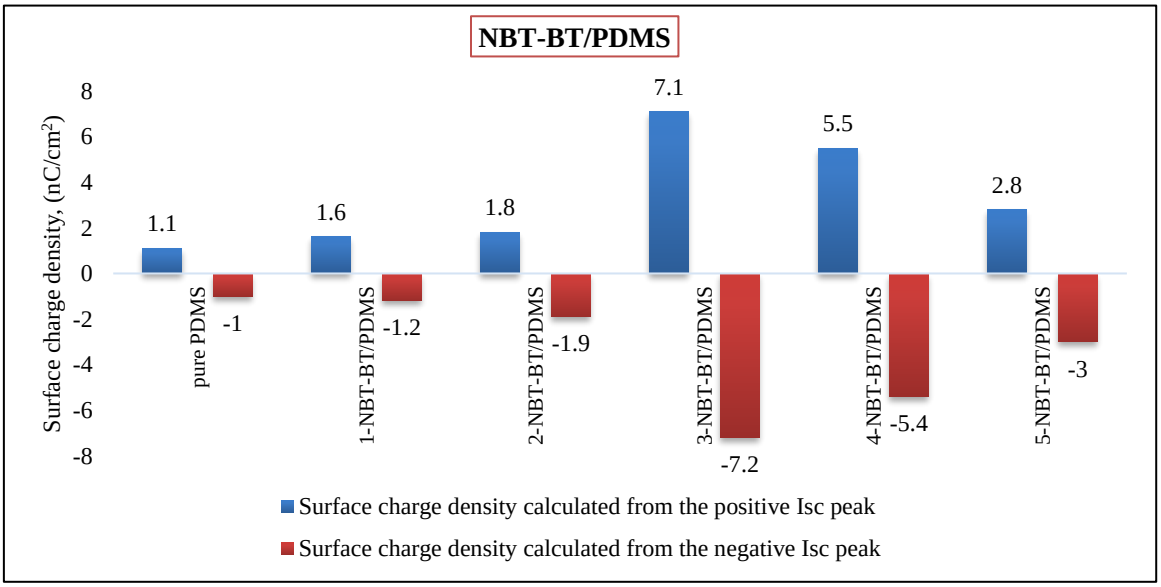

Figure 17. Positive and Negative surface charge densities of pure PDMS and **80**NBT-20BT/PDMS composites calculated from short circuit current (I_{sc}) peaks.

The surface charge density comparison for all $BaTiO_3$/PDMS composite materials is shown in Figure 18 based on both the positive and negative peaks of the short circuit current. As can be observed from the above discussed Figure 17, pure PDMS exhibits a surface charge density of about 1.1/ -1.0 nC/cm^2. With the addition of $BaTiO_3$ powder into the PDMS, the surface charge density value significantly increases across the different samples. In the case of the 1-$BaTiO_3$/PDMS sample, the calculated data corresponds to the value of 2.84/ -2.63 nC/cm^2. The performance reaches its peak with the 2-$BaTiO_3$/PDMS sample, where the highest value of surface charge density is attained at 5.58/ -4.42 nC/cm^2. But, for the 3-$BaTiO_3$/PDMS sample, the surface charge density decreases to 4.53/ -4.24 nC/cm^2. The graph clearly indicates that the configuration of 2-$BaTiO_3$/PDMS is the best for increasing the transfer of charge.

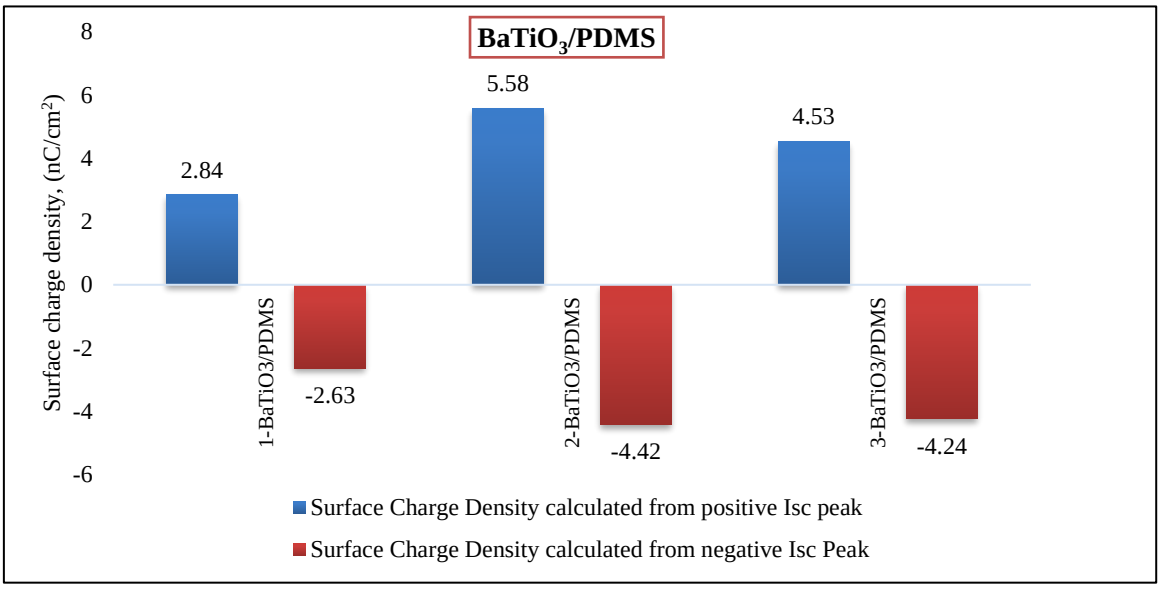

Figure 18. Positive and Negative surface charge densities of pure PDMS and $BaTiO_3$/PDMS composites calculated from short circuit current (I_{sc}) peaks.

When comparing the results of 80NBT-20BT/PDMS and $BaTiO_3$/PDMS, it can be seen that even though $BaTiO_3$ enhances the performance as compared to pure PDMS, the surface charge densities in the case of 80NBT-20BT (specifically 3-NBT-BT at 7.1nC/cm^2) are still higher. This proves that whereas $BaTiO_3$ is an effective material for enhancing the flow of charges, NBT-BT remains more efficient to maximize the total charge density of the triboelectric nanogenerator (TENG) device.

3.5 Load Voltage and Load Current

Figure 19 comprehensively illustrates the simultaneous root mean square (RMS) voltage and RMS current output characteristics of the 1-NBT-BT/PDMS nanogenerator as a function of varying

external load resistance. The RMS value of a signal represents its accurate magnitude and is equal to the value of a constant DC voltage or current that gives the same amount of power to a resistive load. The RMS voltage V_{RMS}, for a time varying voltage $v(t)$ over a period T is defined as:

$$V_{RMS} = \sqrt{\frac{1}{T}\int_0^T [v(t)^2]dt} \tag{3.4}$$

Similarly, the RMS current I_{RMS} is determined in the same way. In Figure 19, the voltage output (pink curve) shows typical behavior: low at small resistances, dramatically increase across the mid resistance range (approximately 10^7 to 10^{10} Ω), and saturating around 14.5 V. Conversely, the current output (teal curve) follows an inverse relationship, beginning at a high value of about 0.11 µA at low resistances and gradually falling as load resistance increases, eventually nearing zero at very high resistances. These curves' distinct intersection and complementary trends demonstrate the change from a current-dominant phase at lower resistances to a voltage-dominant domain at higher resistances. This extensive characterization is critical for identifying the device's effective working range and optimal load impedance at which it can efficiently supply electricity.

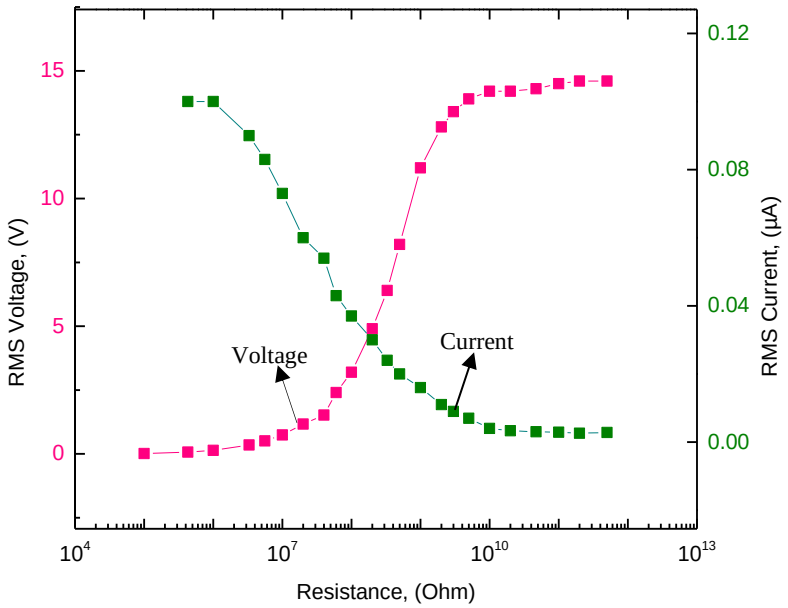

Figure 19. Output Voltage and Current against Load Resistance for a 1-NBT-BT/PDMS TENG

Figure 20(a) demonstrates the RMS voltage output versus external load resistance for pure PDMS and 80NBT-20BT/PDMS composite nanogenerators. The results of all samples have shown

a typical curve in which the voltage rises up to a certain resistance value and then saturates. It is observed that the output voltage generated by 80NBT-20BT/PDMS materials is much greater than that of pure PDMS. The maximum voltage output is recorded as 24.3V from the 4-NBT-BT/PDMS material. This peak is followed by 5-NBT-BT/PDMS at 21.9V, 3-NBT-BT/PDMS at 20.3V, and 2-NBT-BT/PDMS at 20V. All of these values represent a substantial improvement over the 1-NBT-BT/PDMS sample's 14.5V and the pure PDMS baseline of 2V. This indicates that the inclusion and specific composition of 80NBT-20BT fillers significantly improve the nanogenerator's voltage generation capability at higher load resistances.

The RMS voltage output versus the change in external load resistance for $BaTiO_3$/PDMS composite materials is shown in Figure 20(b). All materials exhibit almost similar behavior as the voltage starts low at lower resistances and increases as the resistance goes up until it reaches its saturation level. Among these samples, 3-$BaTiO_3$/PDMS composite generates the best performance with a saturated voltage peak of 25.8V. Next is 2-$BaTiO_3$/PDMS with a saturated voltage of 22.5V, while the 1-$BaTiO_3$/PDMS has the minimum saturation value of around 19.1V, and pure PDMS, as shown in Figure 20(b), only generates a small output of 2V.

By comparing the 80NBT-20BT/PDMS and $BaTiO_3$/PDMS graphs, it can be noted that $BaTiO_3$ performs very well at higher load resistances. Moreover, the highest RMS voltage of the $BaTiO_3$ material (25.8V) even slightly exceeds the highest RMS voltage of the 80NBT-20BT material (24.3V). This clearly demonstrates that the mixing of $BaTiO_3$ and PDMS is very efficient in terms of the RMS output voltage at high resistive loads.

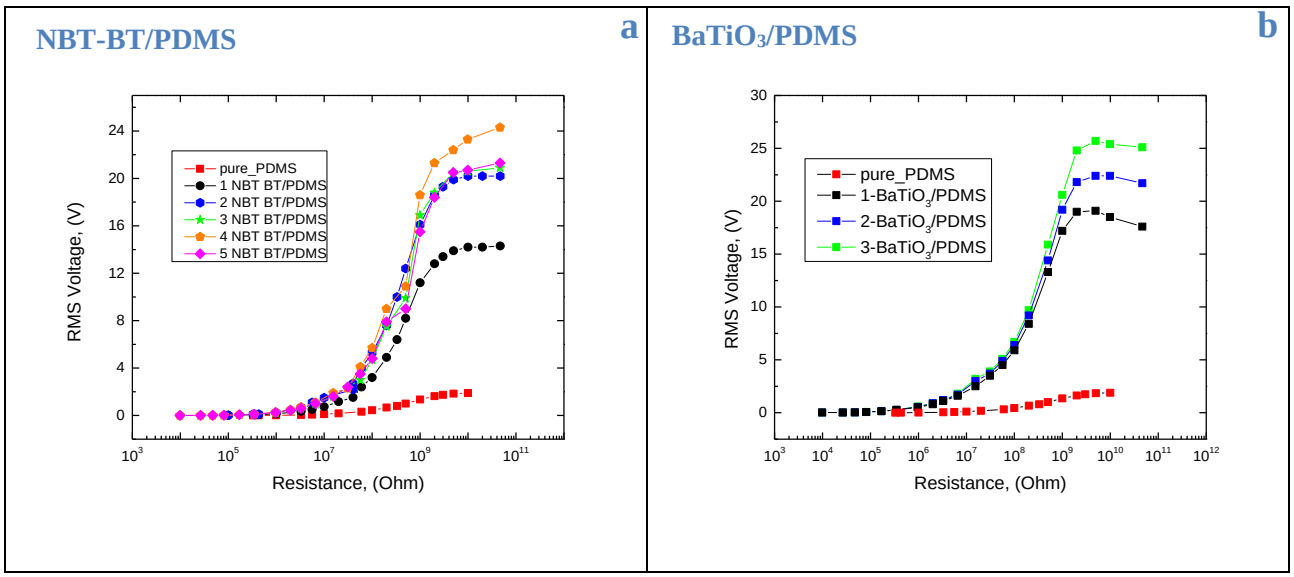

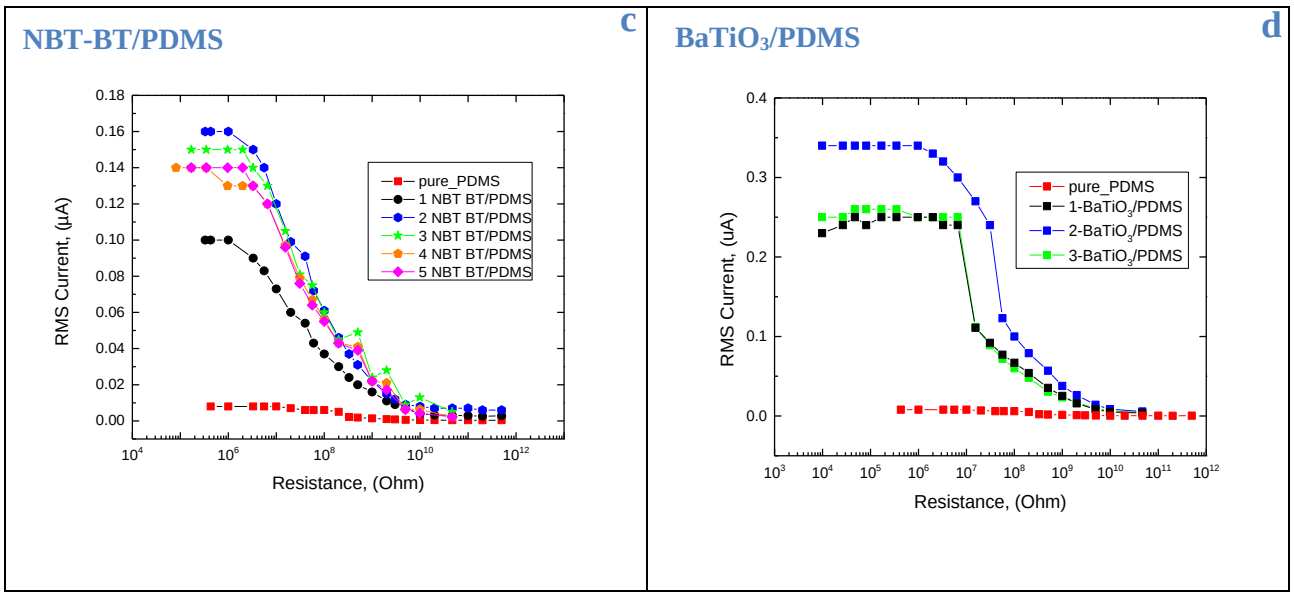

Figure 20. **(a)** Voltage vs Load Resistance for 80NBT-20BT/PDMS (all compositions: pure PDMS, 1-5 NBT-BT/PDMS), **(b)** Voltage vs Load Resistance for $BaTiO_3$/PDMS (all compositions: pure PDMS, 1-3 $BaTiO_3$/PDMS), **(c)** Current vs Load Resistance for 80NBT-20BT/PDMS (all compositions: pure PDMS, 1-5 NBT-BT/PDMS), and **(d)** Current vs Load Resistance for $BaTiO_3$/PDMS (all compositions: pure PDMS, 1-3 $BaTiO_3$/PDMS) by applying a repeated vertical compression force (F) of approximately 20 N with a frequency range of 1 Hz.

Figure 20(c) illustrates the RMS current output of the nanogenerator samples as a function of external load resistance. A characteristic trend is observed where the current is highest at low resistances and gradually decreases with increasing load. The addition of 80NBT-20BT particles significantly increases the current output, which is consistent with voltage observations. Pure PDMS produces approximately 0.006 µA for low resistance values, while 1-NBT-BT/PDMS reaches 0.10 µA. The 2-NBT-BT/PDMS achieves the highest current of 0.16 µA, followed by 3-NBT-BT/PDMS at 0.15 µA, and both 4-NBT-BT/PDMS and 5-NBT-BT/PDMS reach 0.14 µA. These results indicate better charge flow capability of the 80NBT-20BT composite nanogenerators, especially at smaller filler particles.

The RMS current output for the samples of $BaTiO_3$/PDMS composite materials is illustrated in Figure 20(d). The graphs show a sharp decrease in current with an increase in load resistance. By comparing the results of $BaTiO_3$/PDMS and pure PDMS, it can be seen that the addition of these fillers greatly enhances the flow of current through the material. Pure PDMS produces a low output of 0.006 µA. However, with the addition of $BaTiO_3$, there is an improvement in the current output. Specifically, the 2-$BaTiO_3$/PDMS sample achieves the highest performance with an RMS current of approximately 0.34 µA. On the other hand, 1-$BaTiO_3$/PDMS and 3-$BaTiO_3$/PDMS samples generate 0.24 µA and 0.26 µA, respectively.

To illustrate this, the comparison between 80NBT-20BT/PDMS and $BaTiO_3$/PDMS shows that the best 80NBT-20BT sample only reached 0.16 µA, while the 2-$BaTiO_3$/PDMS sample doubles that performance by reaching 0.34 µA. This confirms that while 80NBT-20BT is strong for voltage, $BaTiO_3$ works much better for maximizing the RMS current output in these nanogenerators.

3.6 Power with Load

The power output (P) of a TENG under ideal conditions was determined using the measured Voltage (V) across the load, as shown in equation (1.12). Figure 21 shows the power density output ($\mu W/cm^2$) of the various nanogenerator samples based on external load resistance. In the graph, the trend lines represent parabolic fits to the experimental power data, exhibiting typical behavior in which power density first increases with resistance as voltage develops across the load. The output reaches an ideal peak when the external load resistance matches the device's internal impedance ($R_{load} = R_{internal}$), and then drops at higher load resistances due to reduced current flow.

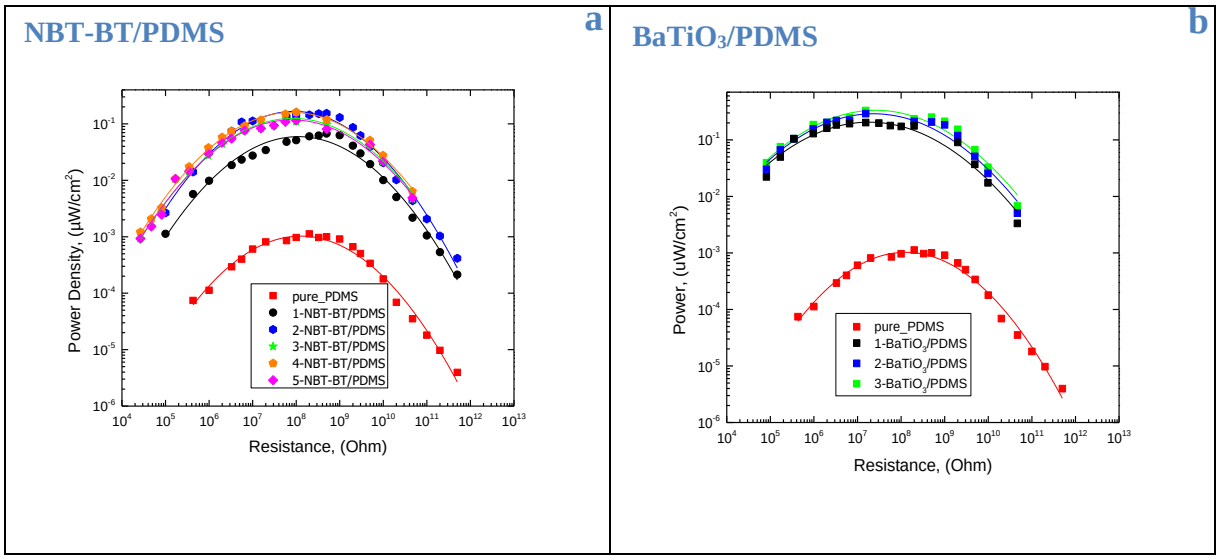

Figure 21. Output Power Density vs Load Resistance for TENGs based on pure PDMS, 80NBT-20BT/PDMS and $BaTiO_3$/PDMS Composites.

The general form of this parabolic fit is given by:

$$P(x) = Ax^2 + Bx + C \tag{3.5}$$

where P is the power output, $y=\log_{10}(P)$, and $x=\log_{10}(R)$ is the logarithm of the load resistance. These coefficients are used to determine R_{max}, the optimal load resistance at which the nanogenerator achieves its maximum power output.

By taking the first derivative of the parabolic power function for x and setting it to zero:

$$\frac{dp}{dx} = 2Ax + B \tag{3.6}$$

The optimal logarithmic resistance x_{max} can be found as:

$$x_{max} = \frac{-\dot{B}}{2A} \tag{3.7}$$

The optimal resistance R_{max} is then calculated as 10^{xmax}.

Table 5, 6 shows coefficients (A, B, C) obtained by fitting the power output vs the logarithm of load resistance data to a parabolic equation (3.5), as well as P_{max} and R_{max} for each nanogenerator sample. This R_{max} value is obtained accurately by determining the maximum point of the parabola.

For pure PDMS, the optimal resistance is 126.77 MΩ. The high value of the resistance suggests that the pure PDMS acts as a good insulating material, which supports the dielectric properties of PDMS. In the case of 80NBT-20BT composites, there is a noticeable drop in the resistance value. Specifically, the resistance drops to 112.46 MΩ for 1-NBT-BT/PDMS and 89.33 MΩ for 2-NBT-BT/PDMS. This decreasing trend continues, where 3-NBT-BT/PDMS exhibits a resistance of 83.18 MΩ, while 4-NBT-BT/PDMS shows a resistance value of 79.94 MΩ, achieving its lowest value at 79.53 MΩ for the 5-NBT-BT/PDMS sample. The decrease in resistance compared to pure PDMS shows that incorporating 80NBT-20BT fillers alters the composite's internal impedance, most likely via interfacial polarization.

As shown in the data (Figure 21(a), Table 5), the incorporation of 80NBT-20BT particles significantly enhances the energy harvesting performance of the composite materials. Pure PDMS exhibits the lowest peak power density, measured at approximately 1.03×10^{-3} μW/cm^2. In comparison, all 80NBT-20BT/PDMS composite samples show a multi magnitude increase in output. Specifically, 1-NBT-BT/PDMS reaches 5.96×10^{-2} μW/cm^2, while 2-NBT-BT/PDMS demonstrates the highest performance of all samples, peaking at 1.66×10^{-1} μW/cm^2. The remaining samples follow this high-performance trend, with 3-NBT-BT/PDMS reaching 1.25×10^{-1} μW/cm^2, 4-NBT-BT/PDMS achieving 1.59×10^{-1} μW/cm^2, and 5-NBT-BT/PDMS outputting 1.17×10^{-1} μW/cm^2. These results indicate that modifying the PDMS matrix with 80NBT-20BT fillers substantially increases the power generation capacity of triboelectric nanogenerators.

Table 5. Optimal resistance and maximum Power data for pure PDMS, 1-NBT-BT/PDMS, 2-NBT-BT/PDMS, 3-NBT-BT/PDMS, 4-NBT-BT/PDMS & 5-NBT-BT/ PDMS.

Samples	**A**	**B**	**C**	**R_{max}, MΩ**	**P_{max}, ($\mu W/cm^2$)**
Pure PDMS	-0.19971	3.23649	-16.10131	126.77	1.03×10^{-3}
1-NBT-BT/PDMS	-0.19087	3.07332	-13.59767	112.46	5.96×10^{-2}
2-NBT-BT/ PDMS	-0.19764	3.14283	-13.27403	89.33	1.66×10^{-1}
3-NBT-BT/ PDMS	-0.17493	2.7709	-11.87576	83.18	1.25×10^{-1}
4-NBT-BT/ PDMS	-0.17775	2.80945	-11.89739	79.94	1.59×10^{-1}
5-NBT-BT/ PDMS	-0.17377	2.74576	-11.77556	79.53	1.17×10^{-1}

Figure 21(b) shows the power density of the $BaTiO_3$/PDMS composite nanogenerator with respect to the resistance of external loads. As can be seen from the figure, it is clear that a general emerges when the power density increases with increasing resistance up to an optimal value (impedance matching), after which it starts to decrease. By comparing the pure PDMS and $BaTiO_3$/PDMS results, it is clear that the addition of fillers has a significant impact on the electrical characteristics of the device. The optimal value of the resistance for pure PDMS is 126.77 MΩ. In contrast, as seen from Table 6, when $BaTiO_3$ is added to the PDMS matrix, there is a sudden decrease in the optimal value of the resistance: 18.72 MΩ for 1-$BaTiO_3$/PDMS, 23.28 MΩ for 2-$BaTiO_3$/PDMS, and 26.13 MΩ for 3-$BaTiO_3$/PDMS, respectively.

With regards to energy harvesting capability, as shown in Figure 21(b), Table 6 confirms that when $BaTiO_3$ is added with PDMS, it leads to a significant improvement in performance as compared to pure PDMS (1.03×10^{-3} μW/cm^2). Specifically, the 3-$BaTiO_3$/PDMS sample achieves the highest peak power density of 3.34×10^{-1} μW/cm^2. While the other two samples (2-$BaTiO_3$/PDMS and 1-$BaTiO_3$/PDMS) show the power density of 2.89×10^{-1} μW/cm^2 and 2.06 μW/cm^2, respectively.

On the comparison of $BaTiO_3$/PDMS and 80NBT-20BT/PDMS materials, $BaTiO_3$ demonstrates a significantly better capability to generate power at much lower optimal resistances. While the best 80NBT-20BT/PDMS sample peaked at 1.66×10−1 μW/cm^2, the 3-$BaTiO_3$/PDMS sample nearly doubles that output. This confirms that $BaTiO_3$ is an exceptionally effective filler for maximizing the power generation of the TENG.

Table 6. Optimal resistance and maximum Power data for 1-$BaTiO_3$/PDMS, 2-$BaTiO_3$/PDMS, and 3-$BaTiO_3$/PDMS

Samples	**A**	**B**	**C**	**R_{max}, MΩ**	**P_{max}, ($\mu W/cm^2$)**
1-$BaTiO_3$	-0.13764	2.0137	-13.65032	18.72	2.06×10^{-1}
2-$BaTiO_3$	-0.14253	2.1087	-13.97182	23.28	2.89×10^{-1}
3-$BaTiO_3$	-0.14159	2.1093	-13.96129	26.13	3.34×10^{-1}

3.7 Capacitance

The value of frequency dependent capacitance obtained from pure PDMS, the five 80NBT-20BT/PDMS composite samples (1 to 5-NBT-BT), and the three $BaTiO_3$/PDMS composite samples (1 to 3-BTO) shows that the capacitance remains constant across the frequency range from 10^2 Hz to 10^6 Hz, which confirms that the material is frequency independent, as shown in Figure 22. All these samples exhibit a consistent and stable behavior across all other composites.

The samples were tested in the "open state" and under various compressive forces. By comparing these fillers to the open state condition (where no pressure is applied and air gaps exist), fillers contribute to a large increase in capacitance, and the amount of capacitance grows even higher with the addition of mechanical forces. This effect occurs because PDMS is a stretchable, elastic material. By applying different forces of 1 N, 5 N, 10 N, 15 N, and 20 N to it, it compresses, which removes the air gaps and reduces the distances between the electrodes.

In open state conditions (the red line), there is a significant air gap, which exhibits low capacitance (just 1.6 pF). However, with different forces starting from 1-N (Black), 5-N (Blue), 10-N (Green), 15-N (Pink), and finally 20-N (Orange) applied, air gaps get compressed, and these composites fill in. Due to high permittivity and reduced layer thickness under applied pressure, the capacitance increases significantly for all composites, ranging from 80 pF to 140 pF. The results indicate that both ceramic fillers significantly boost the charge storage capacity under compression conditions. Thus, we conclude that fillers and applied forces both play an important role here to boost the triboelectric nanogenerators (TENGs) performance.

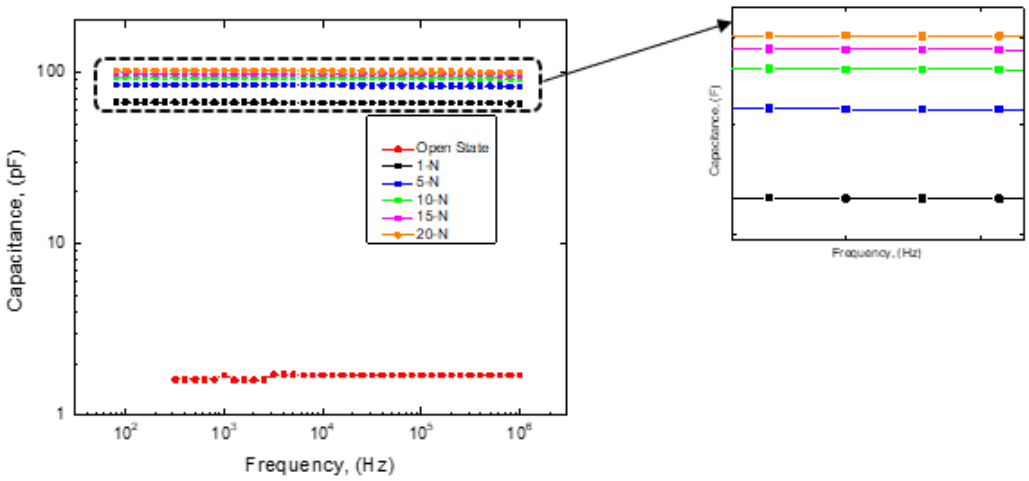

Figure 22. Frequency dependent capacitance of a representative composite sample (4-NBT-BT) under varying mechanical loads, showing a stable trend observed across all samples.

The capacitance for pure PDMS, 80NBT-20BT/PDMS (1-5), and $BaTiO_3$/PDMS (1-3) composites was measured over a wide frequency range. However, to analyze the results more clearly, the values were fixed at a frequency of 10kHz with different forces. As shown in the graphs (Figure 23(a),(b)), the capacitance for each sample increases as the force increases, from 1 N to 20 N. It proves that it is compressed when force is applied to the flexible PDMS matrix; therefore, the distance between two electrodes decreases by the reduced thickness of the composite layer and the absence of inner air gaps. Pure PDMS has the lowest capacitance value, while the others show significantly higher values, confirming that it is mainly based on the high dielectric permittivity of the ceramics and the reduction of the distance by applied force to increase the energy storage capacity.

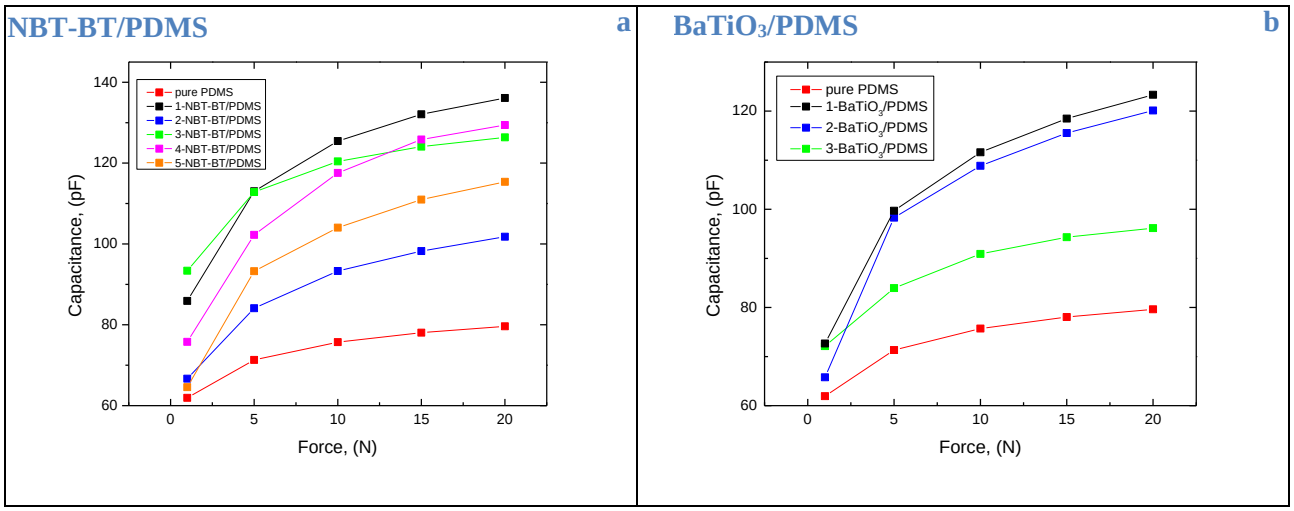

Figure 23. Variation of capacitance as a function of applied force (0.1kg to 2.0kg) for **(a)** pure PDMS and 80NBT-20BT/PDMS composites, and **(b)** pure PDMS and $BaTiO_3$/PDMS composites at 10kHz.

3.8 Dielectric Permittivity

Dielectric permittivity of a material indicates its ability to store electrical energy and polarize in the presence of an electric field. The dielectric permittivity of all samples, including pure PDMS, 80NBT-20BT/PDMS, and $BaTiO_3$/PDMS, was obtained by using the measured capacitance along with the physical dimensions of the samples. The permittivity was obtained from equation (1.3):

$$\varepsilon_r = \frac{Cd}{\varepsilon_o A} \tag{3.8}$$

where d is the thickness of the composite layer, A is the area of the electrode, and ε_o is the permittivity of free space (8.85 x 10^{-12}F/m).

This analysis helps to determine how much the ceramic fillers boost the electric capacity of the PDMS matrix. The resulting graphs show that the dielectric constant remains steady across a frequency range of 10^2 Hz to 10^6 Hz for the pure PDMS, the five 80NBT-20BT/PDMS samples (1 to 5-NBT-BT), and the three $BaTiO_3$/PDMS samples (1 to 3-BTO). As seen in Figure 24(a), the value remains constant for pure PDMS at the base level of 2.7, but when 80NBT-20BT fillers are added with PDMS, the permittivity of the sample with 3-NBT-BT (Green) reaches the maximum value of 4.8, while other samples have values ranging from 3.3 to 3.9. Similarly, when pure PDMS is mixed with $BaTiO_3$ as given in Figure 24(b), the fillers give a significant boost. While 2-BTO (Blue) and 1-BTO (Black) retain constant values around 3.0 and 3.7, the 3-BTO (Green) sample attains the highest permittivity of 4.9. This stability shows that both 80NBT-20BT and BTO-filled PDMS composites are highly dependable for reliable and consistent electrical performance across a wide range of applications.

As can be observed from the comparison of both fillers, it is clear that $BaTiO_3$/PDMS shows better performance than 80NBT-20BT/PDMS. The highest value of permittivity for the $BaTiO_3$/PDMS composite is 4.9 compared to 4.8 for 80NBT-20BT/PDMS. Additionally, the $BaTiO_3$ samples showed more stability across high frequencies, which makes it a better choice for increasing the charge storage and improving the power of TENG devices.

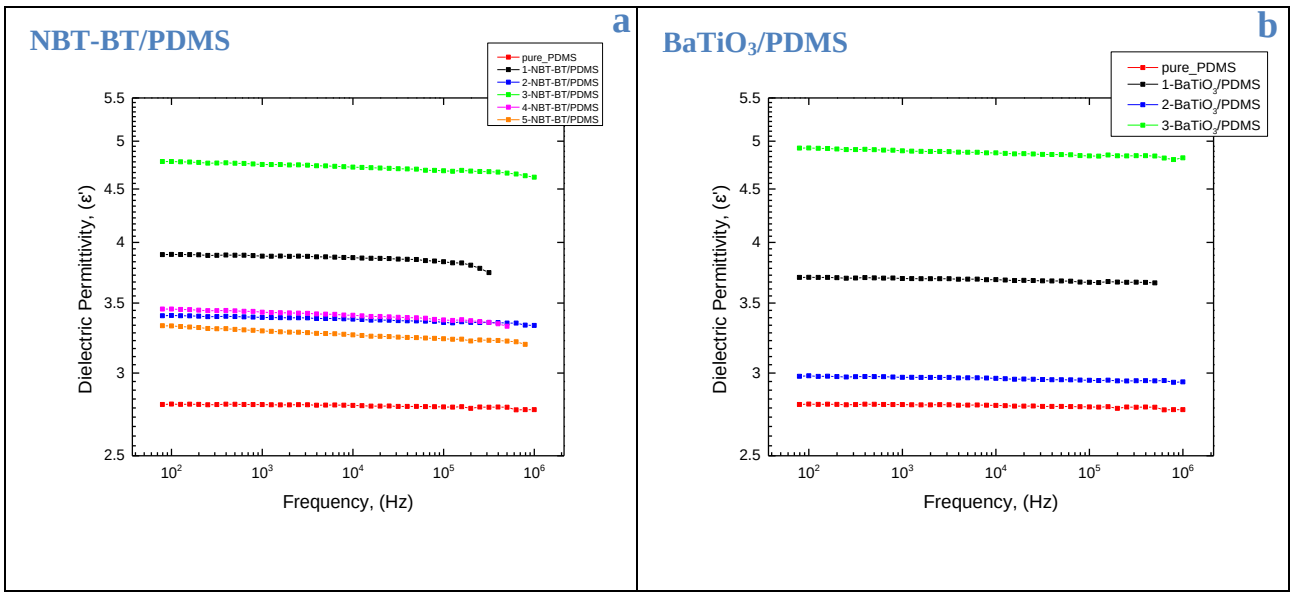

Figure 24. Frequency-dependent dielectric permittivity (ε_r) for **(a)** pure PDMS and various 80NBT-20BT/PDMS composites, and **(b)** pure PDMS and various $BaTiO_3$/PDMS composites representing the stability of the dielectric constant across a broad frequency range.

CONCLUSIONS

The main conclusions of the work are following:

- The incorporation of ferroelectric fillers (80NBT-20BT and $BaTiO_3$ of different sizes) at 47wt% into PDMS significantly improved the short circuit current, Isc, and positive/negative surface charge density from 1.2 µA and 1.1/-1.0 nC/cm^2 (for pure PDMS) to 7.2 µA and 7.1/-7.2 nC/cm^2 (for 3-NBT-BT), and to 7.7 µA and 5.58/-4.42 nC/cm^2 (for 2-$BaTiO_3$), respectively.
- The 3-$BaTiO_3$/PDMS-based TENG achieved a higher peak power density of 3.34×10^{-1} µW/cm² (at R_{max} of 26.13 MΩ), nearly double the highest output of 1.66×10^{-1} µW/cm² for 2-NBT-BT/PDMS (at R_{max} of 89.33 MΩ). For pure PDMS, the maximum power density of 1.03×10^{-3} µW/cm² is observed at R_{max} of 126.77 MΩ.
- All samples exhibited frequency independent capacitance; applied forces (up to 20 N) increased the capacitance from an open state value of 1.6 pF into the 80 pF to 140 pF range for all composite samples, by reducing air gaps. Ceramic fillers increased the dielectric permittivity from 2.7 (pure PDMS) to a maximum of 4.9 (3-$BaTiO_3$/PDMS).

REFERENCES

1. Lin, Z., Chen, J., & Yang, J. (2016). Recent progress in triboelectric nanogenerators as a renewable and sustainable power source. Journal of Nanomaterials, 2016(1), 5651613. https://doi.org/10.1155/2016/5651613
2. Yang, Y., Zhu, G., Zhang, H., Chen, J., Zhong, X., Lin, Z. H., ... & Wang, Z. L. (2013). Triboelectric nanogenerator for harvesting wind energy and as self-powered wind vector sensor system. ACS nano, 7(10), 9461-9468. https://doi.org/10.1021/nn4043157
3. Li, G. Z., Wang, G. G., Cai, Y. W., Sun, N., Li, F., Zhou, H. L., ... & Yang, Y. (2020). A high-performance transparent and flexible triboelectric nanogenerator based on hydrophobic composite films. Nano Energy, 75, 104918. https://doi.org/10.1016/j.nanoen.2020.104918
4. Chen, J., Guo, H., He, X., Liu, G., Xi, Y., Shi, H., & Hu, C. (2016). Enhancing performance of triboelectric nanogenerator by filling high dielectric nanoparticles into sponge PDMS film. ACS applied materials & interfaces, 8(1), 736-744. https://doi.org/10.1021/acsami.5b09907
5. Su, H., Wang, X., Li, C., Wang, Z., Wu, Y., Zhang, J., ... & Zheng, H. (2021). Enhanced energy harvesting ability of polydimethylsiloxane-$BaTiO_3$-based flexible piezoelectric nanogenerator for tactile imitation application. Nano Energy, 83, 105809. https://doi.org/10.1016/j.nanoen.2021.105809
6. Scarisoreanu, N. D., Birjega, R., Andrei, A., Dinescu, M., Craciun, F., & Galassi, C. (2012). Phase transitions, dielectric and ferroelectric properties of lead-free NBT-BT thin films. Advances in Ferroelectrics. http://dx.doi.org/10.5772/52187
7. Lazar, K. A., Vijoy, K. V., Joseph, T., John, H., & Saji, K. J. (2023). Vertically integrated triboelectric nanogenerators using PDMS/LSCO composite. Materials Science and Engineering: B, 292, 116388. https://doi.org/10.1016/j.mseb.2023.116388
8. Paranjape, M. V., Kim, J., Kim, Y., Jo, E., Graham, S. A., Manchi, P., ... & Yu, J. S. (2023). Perovskite V–NaNbO3 embedded PDMS composite film-based robust hybrid nanogenerator for efficient mechanical energy harvesting. Composites Science and Technology, 242, 110195. https://doi.org/10.1016/j.compscitech.2023.110195

9. Lee, K., Ryu, J. H., Han, H., Kim, B., Jung, K., Moon, I. Y., ... & Kim, K. M. (2025). Boosting triboelectric performance of PDMS-based nanogenerators through dual-filler embedded triboelectric layers. Journal of Alloys and Compounds, 1010, 177114. https://doi.org/10.1016/j.jallcom.2024.177114
10. Park, H. W., Huynh, N. D., Kim, W., Lee, C., Nam, Y., Lee, S., ... & Choi, D. (2018). Electron blocking layer-based interfacial design for highly-enhanced triboelectric nanogenerators. Nano Energy, 50, 9-15. https://doi.org/10.1016/j.nanoen.2018.05.024
11. Zhao, K., Zhang, X., Lv, H., Sun, W., Zhong, M., Liu, M., ... & Zhang, D. (2022). Boosting performance of triboelectric nanogenerator via polydimethylsiloxane modified with perovskite BiFeO3 nanoparticles. Materials Technology, 37(14), 3212-3221. https://doi.org/10.1080/10667857.2022.2138804
12. Sahu, M., Hajra, S., Bijelic, J., Oh, D., Djerdj, I., & Kim, H. J. (2021). Triple perovskite-based triboelectric nanogenerator: a facile method of energy harvesting and self-powered information generator. Materials today energy, 20, 100639. https://doi.org/10.1016/j.mtener.2021.100639
13. Wang, S., Lin, L., & Wang, Z. L. (2012). Nanoscale triboelectric-effect-enabled energy conversion for sustainably powering portable electronics. Nano letters, 12(12), 6339-6346. https://doi.org/10.1021/nl303573d
14. Xu, L., Hasan, M. A. M., Wu, H., & Yang, Y. (2021). Electromagnetic–triboelectric hybridized nanogenerators. Energies, 14(19), 6219. https://doi.org/10.3390/en14196219
15. Niu, S., & Wang, Z. L. (2015). Theoretical systems of triboelectric nanogenerators. Nano Energy, 14, 161-192. https://doi.org/10.1016/j.nanoen.2014.11.034
16. Zhang, W., Shi, Y., Li, Y., Chen, X., & Shen, H. (2022). A review: Contact electrification on special interfaces. Frontiers in Materials, 9, 909746. https://doi.org/10.3389/fmats.2022.909746
17. Li, X., Wei, D., & Wang, Z. L. (2023). Direct current triboelectric nanogenerators, a perspective from material selections. Nanoenergy Advances, 3(4), 343-375. https://doi.org/10.3390/nanoenergyadv3040018
18. Wu, C., Wang, A. C., Ding, W., Guo, H., & Wang, Z. L. (2019). Triboelectric nanogenerator: a foundation of the energy for the new era. Advanced Energy Materials, 9(1), 1802906. https://doi.org/10.1002/aenm.201802906

19. Wang, Z. L. (2023). Introduction to triboelectric nanogenerators. In Handbook of Triboelectric Nanogenerators (pp. 3-32). Cham: Springer International Publishing. https://doi.org/10.1007/978-3-031-28111-2_1
20. Kang, X., Li, P., Yurchenko, D., Dai, S., & Wang, J. (2025). Fundamental theory and cutting-edge applications of TENGs. Materials Futures, 4(4), 042101. https://doi.org/10.1088/2752-5724/adf132
21. Doganay, D., Durukan, M. B., Cugunlular, M., Cakir, O., Cicek, M. O., Demircioglu, O., ... & Unalan, H. E. (2025). Triboelectric nanogenerators from fundamentals to applications. Nano Energy, 138, 110825. https://doi.org/10.1016/j.nanoen.2025.110825
22. Niu, S., Wang, S., Lin, L., Liu, Y., Zhou, Y. S., Hu, Y., & Wang, Z. L. (2013). Theoretical study of contact-mode triboelectric nanogenerators as an effective power source. Energy & Environmental Science, 6(12), 3576-3583. https://doi.org/10.1039/C3EE42571A
23. Wang, Z. L., & Wang, A. C. (2019). On the origin of contact-electrification. Materials Today, 30, 34-51. https://doi.org/10.1016/j.mattod.2019.05.016
24. Wang, Z. L. (2013). Triboelectric nanogenerators as new energy technology for self-powered systems and as active mechanical and chemical sensors. ACS nano, 7(11), 9533-9557. https://doi.org/10.1021/nn404614z
25. Zhou, L., Liu, D., Wang, J., & Wang, Z. L. (2020). Triboelectric nanogenerators: fundamental physics and potential applications. Friction, 8(3), 481-506. https://doi.org/10.1007/s40544-020-0390-3
26. Zou, H., Zhang, Y., Guo, L., Wang, P., He, X., Dai, G., ... & Wang, Z. L. (2019). Quantifying the triboelectric series. Nature communications, 10(1), 1427. https://doi.org/10.1038/s41467-019-09461-x
27. Kim, Y. J., Lee, J., Park, S., Park, C., Park, C., & Choi, H. J. (2017). Effect of the relative permittivity of oxides on the performance of triboelectric nanogenerators. RSC advances, 7(78), 49368-49373. https://doi.org/10.1039/C7RA07274K
28. Zou, H., Guo, L., Xue, H., Zhang, Y., Shen, X., Liu, X., ... & Wang, Z. L. (2020). Quantifying and understanding the triboelectric series of inorganic non-metallic materials. Nature communications, 11(1), 2093. https://doi.org/10.1038/s41467-020-15926-1

29. Simon, P., & Gogotsi, Y. (2008). Materials for electrochemical capacitors. Nature materials, 7(11), 845-854. https://doi.org/10.1038/nmat2297
30. Choi, G. J., Sohn, S. H., Kim, S. J., & Park, I. K. (2025). Polymer composite-based triboelectric nanogenerators: recent progress, design principles, and future perspectives. Polymers, 17(14), 1962. https://doi.org/10.3390/polym17141962
31. Bhalla, A. S., Guo, R., & Roy, R. (2000). The perovskite structure—a review of its role in ceramic science and technology. Materials research innovations, 4(1), 3-26. https://doi.org/10.1007/s100190000062
32. Jiao, H., Jin, J., Zhao, K., Zhou, X. R., Zhang, X., Song, S., ... & Cui, G. (2023). Synthesis and piezoelectric photocatalytic, mechanical, and electrical properties of porous t-$BaTiO_3$/Ag/β-PVDF composite material. Journal of Thermoplastic Composite Materials, 36(5), 2031-2049. https://doi.org/10.1177/08927057221088466
33. Li, Z., Zheng, Q., Wang, Z. L., & Li, Z. (2020). Nanogenerator-based self-powered sensors for wearable and implantable electronics. Research. https://doi.org/10.34133/2020/8710686
34. Wang, J. J., Meng, F. Y., Ma, X. Q., Xu, M. X., & Chen, L. Q. (2010). Lattice, elastic, polarization, and electrostrictive properties of $BaTiO_3$ from first-principles. Journal of Applied Physics, 108(3). https://doi.org/10.1063/1.3462441
35. K. Riaz, K. Khelif, and M. U. Bukhari, "Green and eco-friendly triboelectric nanogenerators," *Nano Energy*, vol. 121, p. 109241, 2024. https://doi.org/10.5772/intechopen.1012346
36. Katta, V., Mohana Rani, G., Umapathi, R., Huh, Y. S., & Sanasi, P. D. (2026). Chitosan-Loaded Lead-Free Sodium Bismuth Titanate Composite Flexible Triboelectric Nanogenerator for Energy Harvesting, Biomechanical Sensing, and Smart-Path Touch-Lighting for Safe Walking Applications. Small, e12352. https://doi.org/10.1002/smll.202512352
37. Mishra, A., Abebe, G., Jafo, G., Das Adhikary, G., & De, A. (2021). Effect of A-site off-stoichiometry on the microstructural, structural, and electromechanical properties of lead-free tetragonal 0.80 $Na_{0.5}Bi0.5TiO3$–0.20 $BaTiO_3$ (NBT–20BT) piezoceramic. Journal of Materials Science: Materials in Electronics, 32(9), 12578-12593. https://doi.org/10.1007/s10854-021-05895-6

38. Wang, Z. L. (2014). Triboelectric nanogenerators as new energy technology and self-powered sensors–Principles, problems and perspectives. Faraday discussions, 176, 447-458. https://doi.org/10.1039/C4FD00159A
39. Fan, F. R., Tian, Z. Q., & Wang, Z. L. (2012). Flexible triboelectric generator. Nano energy, 1(2), 328-334. https://doi.org/10.1016/j.nanoen.2012.01.004
40. Parida, K., Kumar, V., Jiangxin, W., Bhavanasi, V., Bendi, R., & Lee, P. S. (2017). Highly transparent, stretchable, and self-healing ionic-skin triboelectric nanogenerators for energy harvesting and touch applications. Advanced Materials, 29(37), 1702181. https://doi.org/10.1002/adma.201702181
41. Li, Q., Liu, W., Yang, H., He, W., Long, L., Wu, M., ... & Wang, Z. L. (2021). Ultra-stability high-voltage triboelectric nanogenerator designed by ternary dielectric triboelectrification with partial soft-contact and non-contact mode. Nano Energy, 90, 106585. https://doi.org/10.1016/j.nanoen.2021.106585
42. Li, S., Fan, Y., Chen, H., Nie, J., Liang, Y., Tao, X., ... & Wang, Z. L. (2020). Manipulating the triboelectric surface charge density of polymers by low-energy helium ion irradiation/implantation. Energy & Environmental Science, 13(3), 896-907. https://doi.org/10.1039/C9EE03307F
43. Nie, J., Ren, Z., Xu, L., Lin, S., Zhan, F., Chen, X., & Wang, Z. L. (2020). Probing contact-electrification-induced electron and ion transfers at a liquid–solid interface. Advanced Materials, 32(2), 1905696. https://doi.org/10.1002/adma.201905696
44. Luo, J., & Wang, Z. L. (2020). Recent progress of triboelectric nanogenerators: From fundamental theory to practical applications. EcoMat, 2(4), e12059. https://doi.org/10.1002/eom2.12059
45. Rajasekar, M., & Sivakumar, M. (2025). Recent trends and future perspectives of triboelectric nanogenerators (TENGs) and applications. RSC advances, 15(57), 49600-49642. https://doi.org/10.1039/D5RA06645J
46. Meisak, D., Plyushch, A., Kinka, M., Balčiūnas, S., Kalendra, V., Schaefer, S., ... & Celzard, A. (2024). Effect of particle size on the origin of electromechanical response in $BaTiO_3$/PDMS nanogenerators. ACS Applied Electronic Materials, 6(10), 7464-7474. https://doi.org/10.1021/acsaelm.4c01333
47. Shanbedi, M., Ardebili, H., & Karim, A. (2023). Polymer-based triboelectric nanogenerators: Materials, characterization, and applications. Progress in Polymer Science, 144, 101723. https://doi.org/10.1016/j.progpolymsci.2023.101723

48. Liang, Y., Ozawa, M., & Krueger, A. (2009). A general procedure to functionalize agglomerating nanoparticles demonstrated on nanodiamond. ACS nano, 3(8), 2288-2296. https://doi.org/10.1021/nn900339s
49. Takahashi, M., Oya, M., & Fuji, M. (2004). Transparent observation of particle dispersion in alumina slurry using in situ solidification. Advanced Powder Technology, 15(1), 97-107. https://doi.org/10.1163/15685520460740098
50. Marković, S., Mitrić, M., Starčević, G., & Uskoković, D. (2008). Ultrasonic de-agglomeration of barium titanate powder. Ultrasonics sonochemistry, 15(1), 16-20. https://doi.org/10.1016/j.ultsonch.2007.07.008

Vilniaus universitetas Fizikos fakultetas
Taikomosios elektrodinamikos ir Telekomunikacijų institutas

Muhammad Shahzaib Asad

PDMS PAGRINDU FERROELEKTRINĖMIS DALELĖMIS UŽPILDYTŲ KOMPOZITŲ TRIBOELEKTRINĖS SAVYBĖS

Magistro baigiamasis darbas

SANTRAUKA

Pasaulinė tvarios ir mažų sąnaudų atsinaujinančios energijos surinkimo paklausa paskatino šį tyrimą, kurio tikslas buvo pagerinti lanksčių PDMS pagrindu veikiančių triboelektrinių nanogeneratorių (TENG) veikimą, naudojant švino neturinčius feroelektrinius užpildus esant 47wt% (80NBT-20BT ir $BaTiO_3$) skirtingų dydžių. Siekiant ištirti 80NBT-20BT dalelių dydžio poveikį, dalelių dydis buvo sumažintas nuo 300 ± 100 nm iki 100 ± 50 nm naudojant planetarinį rutulinį malimą. Buvo naudojami trijų dydžių (700nm, 300nm ir 80nm) $BaTiO_3$. Eksperimentiniai rezultatai rodo didelį triboelektrinės išvesties pagerėjimą, palyginti su grynu PDMS. Trumpojo jungimo srovė, Isc, ir teigiamo/neigiamo paviršiaus krūvio tankis padidėjo nuo 1.2 µA ir 1.1/-1.0 nC/cm^2 (grynam PDMS) iki 7.2 µA ir 7.1/ -7.2 nC/cm^2 (80NBT-20BT), ir iki 7.7 µA bei 5.58/-4.42 nC/cm^2 ($BaTiO_3$), atitinkamai. Tarp užpildų, 80nm dydžio $BaTiO_3$ dalelės parodė didesnį maksimalų galios tankį – 0.334 µW/cm² (esant R_{max} 26.13 MΩ) ir aukštą dielektrinę skvarbą – 4.9. Be to, buvo parodyta, kad taikoma jėga padidina talpą nuo 1.6 pF gryno PDMS iki 80 pF iki 140 pF visiems kompozitiniams mėginiams, kai sumažėja vidiniai oro tarpai, užtikrinant pagerintą krūvio kaupimo stabilumą. Šie rezultatai rodo, kad optimizuoti kompozitai yra idealūs savaime maitinamiems dėvimiesiems elektroniniams įrenginiams, biomechaniniams jutikliams ir aplinkos energijos surinkimo taikymams.

Vilnius University Faculty of Physics
Institute of Applied Electrodynamics and Telecommunications

Muhammad Shahzaib Asad

TRIBOELECTRIC PROPERTIES OF PDMS-BASED COMPOSITES FILLED WITH FERROELECTRIC PARTICLES

Master's thesis

SUMMARY

The demand for sustainable and low cost renewable energy harvesting on a global scale has driven this research aimed to improve the performance of flexible PDMS based triboelectric nanogenerators (TENGs) using lead free ferroelectric fillers at 47wt% (80NBT-20BT and $BaTiO_3$) of different sizes. To investigate the 80NBT-20BT particle size effect, the particle size was reduced from 300 ± 100 nm to 100 ± 50 nm by planetary ball milling. Three particle sizes (700nm, 300nm, and 80nm) of $BaTiO_3$ were used. The experimental results show a great improvement in the triboelectric output compared to pure PDMS. The short circuit current, Isc, and positive/negative surface charge density increased from 1.2 µA and 1.1/-1.0 nC/cm^2 (for pure PDMS) to 7.2 µA and 7.1/-7.2 nC/cm^2 (for 80NBT-20BT), and to 7.7 µA and 5.58/-4.42 nC/cm^2 (for $BaTiO_3$), respectively. Among the fillers, $BaTiO_3$ particles of 80nm in size showed a higher peak power density of 0.334 µW/cm² (at R_{max} of 26.13 MΩ) and a high dielectric permittivity of 4.9. Furthermore, the applied force was demonstrated to increase the capacitance from 1.6 pF pure PDMS into 80 pF to 140 pF for all composite samples, as the internal air gaps decreased, providing enhanced charge storage stability. These results show that the optimized composites are ideal for self-powered wearable electronic devices, biomechanical sensors, and environmental energy harvesting applications.